

Elevated foehn exacerbates surface ozone pollution in summer Beijing

Zhiheng Liao¹, Jing Xu¹, Ju Li¹, Liyan Zhou¹, Chao Liu¹, Lin Wu², Zhiqiang Ma¹

¹Institute of Urban Meteorology, China Meteorological Administration, Beijing, China;

²Huairou Meteorological Office of Beijing, Beijing, China.

Correspondence: Z. Liao (zhliao@ium.cn) and Z. Ma (zqma@ium.cn)

Abstract: While several studies have evaluated the impact of shallow foehn on air pollution, the effects of elevated foehn on O₃ pollution remain poorly understood. Here, we investigate the role of elevated foehn in summer O₃ pollution in Beijing through detailed case analysis and a long-term climatological evaluation. The case study reveals that elevated foehn exacerbates next-day O₃ pollution through three primary mechanisms: first, by increasing boundary layer temperature, thereby enhancing photochemical O₃ formation; second, by reducing the residual/boundary layer height, thereby inhibiting vertical diffusion of pollutants; and third, by slowing boundary layer winds, thereby suppressing horizontal dispersion. A ten-year climatological evaluation of 54 identified elevated foehn events strongly supports these mechanisms. On average, these events led to a post-foehn afternoon boundary layer temperature increase exceeding 3°C, an afternoon boundary layer height reduction of more than 100 m, and a decrease in afternoon boundary layer wind speed of more than 1.0 m s⁻¹ compared to the pre-foehn days. Consequently, 87% of elevated foehn events were associated with a worsening of O₃ pollution. Post-foehn daily maximum 8-hour average O₃ concentrations frequently surpassed the national pollution threshold (160 µg m⁻³), with an average increase of 20%–60% (varying by site and higher in urban areas) compared to preceding days. These results demonstrate a robust and deterministic exacerbating effect of elevated foehn on surface O₃ pollution, suggesting that elevated foehn can serve as a reliable meteorological precursor for O₃ pollution warnings in summer Beijing.

Keywords: elevated foehn, atmospheric boundary layer, residual layer warming, ozone pollution, Beijing

1. Introduction

Foehn is a phenomenon of downslope winds with significant warming on the mountain leeward side (Elvidge and Renfrew, 2016). It has been observed among many large mountains in the world, including the Alpine Mountains (Miltenberger et al., 2016; Seibert et al., 2000), Rocky Mountains (Kerr, 1986), Appalachian Mountains (Gaffin, 2002, 2009), Taihang Mountains (Li et al., 2020a; Li et al., 2025), and Tianshan Mountains (Li et al., 2015; Li et al., 2020b). The societal and economic impacts of foehn winds are wide-ranging and well-documented, encompassing enhanced fire risks, extreme heat exposure, impacts on air quality, beneficial impacts on agriculture, and direct wind-driven damage to infrastructure. Given these multifaceted impacts, foehn has long been a subject of sustained scholarly interest across diverse disciplines.

Scientific research into the effect of foehn on air pollution began in Europe in the late nineteenth century, primarily to explain elevated ozone (O₃) levels in the Alpine regions during foehn events (Baumann et al., 2001; Campana et al., 2005; Seibert et al., 2000). Early European studies identified that the initial rise in O₃ concentration was caused by the advection of residual-layer air masses from source regions such as the Po Basin. Later on, O₃ levels in the foehn-affected area were found to be influenced by regional-scale advection from the lower free troposphere or even the stratosphere. Collectively, these studies emphasized the transport role of foehn in

45 influencing O₃ air quality in the relatively clean valleys of Alps. In contrast, research in China has commonly
46 demonstrated a “clearance effect” of foehn on air pollution in highly-polluted cities (Li et al., 2020a; Li et al., 2025;
47 Yang et al., 2018). For example, Yang et al. (2018) reported a case in Shijiazhuang where foehn led to rapidly
48 improved horizontal visibility, decreased aerosol concentration, and weakened haze intensity. Similarly, a six-year
49 statistical study by Li et al. (2025) found that 60.4 % of foehn events were associated with a subsequent decrease in
50 fine particulate matter (PM_{2.5}) concentrations in Beijing. This clearance effect is attributed to the origin of the foehn
51 winds, which typically transport cleaner air from the less polluted western, northwestern and northern mountain
52 areas of the Hebei–Beijing region into more polluted plains.

53

54 These abovementioned studies, conducted in both Europe and China, primarily examine the foehn effect on air
55 pollution mainly from a dynamical (transport) perspective. Furthermore, the foehn cases selected in these studies
56 are generally confined to shallow foehns, identifying using near-surface meteorological observations. Crucially,
57 however, the defining feature of foehn is the associated warming (Elvidge and Renfrew, 2016). This warming
58 inevitably alters the vertical thermal structure—and thus the atmospheric stability—which directly governs the
59 capacity for vertical diffusion of air pollutants (Liao et al., 2018; Stull, 1988). Therefore, the vertical extent of the
60 foehn (shallow or elevated) critically determines its impact on atmospheric stability: shallow foehn tends to
61 enhance near-surface instability, while elevated foehn can strengthen stability within or above the boundary layer.
62 From this thermodynamic perspective, elevated foehn likely possesses a greater pollution potential than its shallow
63 counterpart. Despite this reasoning, to the best of our knowledge, only one study—Li et al. (2015) in Urumqi, a city
64 adjacent to Tianshan Mountains—has explicitly investigated the impact of an elevated foehn on air pollution from a
65 thermodynamic viewpoint. That study revealed that an elevated southeasterly foehn layer between 480 and 2100 m
66 created a very stable boundary layer structure, which suppressed vertical mixing and led to severe haze pollution
67 episodes. Recent studies on PM_{2.5} pollution in Beijing (Li et al., 2020a; Li et al., 2025) have speculated that
68 post-foehn pollution exacerbation might be driven by a mechanism similar to the elevated foehn process observed
69 in Urumqi (Li et al., 2015). However, the existence and role of such an elevated foehn mechanism have not yet
70 been observationally confirmed for Beijing.

71

72 Beijing, the capital of China, faces significant challenges in terms of air pollution. Particularly in recent summers,
73 O₃ has surpassed PM_{2.5} as the most important air pollutant, arousing widespread attention (Liao et al., 2023; Zong
74 et al., 2023). The city’s location on the plains adjacent to the Taihang Mountains to the west and the Yan Mountains
75 to the north makes it particularly susceptible to foehn winds (Xu et al., 2026). Luo et al. (2020) documented an
76 intensive foehn warming event in Beijing where nocturnal air temperatures increased by over 10°C per hour.
77 Utilizing data from a density automatic weather station network, Li et al. (2025) developed a foehn identification
78 method and reported an annual average of 56.5 foehn days in Beijing. As noted earlier, their statistical analysis
79 suggests a higher probability of PM_{2.5} pollution alleviation (60.4 %) rather than pollution exacerbation (39.6 %)
80 following foehn events in Beijing. Importantly, because their identification method only relies on near-surface
81 observations, the detected events are predominantly shallow foehns. This methodological focus may obscure the
82 distinct air pollution effects potentially caused by elevated foehns. Therefore, determining whether elevated foehn
83 induces a more deterministic—and likely adverse—pollution effects is a critical unanswered question. The answer
84 has practical importance, as it would inform whether elevated foehn can serve as a reliable precursor indicator for
85 air pollution warnings, thereby improving mitigation efforts in Beijing and other leeside cities.

86

87 To address this knowledge gap, our team deployed two O₃ lidars at an urban (Guanxiangtai, GXT) and a rural
88 (Shangdianzi, SDZ) station in Beijing in late July 2024. This coordinated dual-station lidar setup is particularly

89 suited to capturing the three-dimensional characteristics and mechanisms of boundary layer O₃ evolution under the
90 influence of elevated foehn. One month after deployment (27–31 August), we observed an O₃ pollution episode
91 associated with an elevated foehn. In this study, we conducted a detailed analysis of this event by integrating data
92 from the new lidar system with co-located remote sensing meteorological observations. We supplement this case
93 study with a climatological evaluation using a decade (2015–2024) of routine observations. Our overarching aim is
94 to elucidate the specific role of elevated foehn in driving summer O₃ pollution in Beijing.

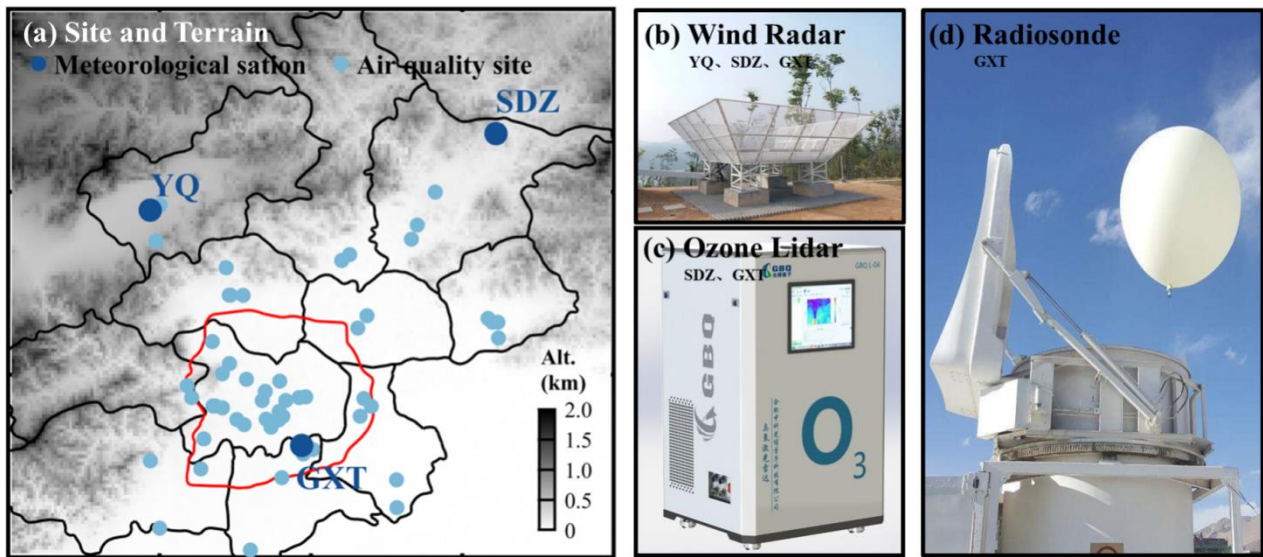
95

96 2. Data and method

97 2.1. Observational data

98 Figure 1 shows the observation network and instruments. The network comprises 3 meteorological stations and
99 46 surface O₃ monitoring sites. Among the O₃ sites, 45 are air quality stations operated by the Beijing Municipal
100 Ecological and Environmental Monitoring Center, and one is the Shangdianzi (SDZ) atmospheric background
101 station managed by the Beijing Meteorological Bureau. Two differential absorption O₃ lidars (Hefei GBQ
102 Technology Company) were deployed at the GXT (urban) and SDZ (rural) stations, respectively. These lidars
103 measured O₃ profiles with a 5-minute resolution up to an altitude of 3.0 km. In addition, radar wind profilers at
104 GXT, SDZ, as well as Yanqing (YQ) provided continuous wind profiles at 6-minute resolution. Routine
105 meteorological radiosondes launched from the GXT station provided high-vertical-resolution (~10 m) profiles of
106 temperature, relative humidity, wind speed, and wind direction three times daily (08:00, 14:00, and 20:00 BJT) in
107 summer.

108



109 **Figure 1.** Site distribution of surface ozone and meteorological measurements, and ground-based remote sensing
110 instruments used in this study. In (a), dark blue dots denote the GXT, SDZ, and YQ meteorological stations; light
111 blue dots represent the surface ozone observation sites. Panels (b), (c), and (d) show the radar wind profilers at YQ,
112 SDZ, and GXT, ozone lidars at SDZ and GXT, and routine radiosonde instrument at GXT, respectively.

113

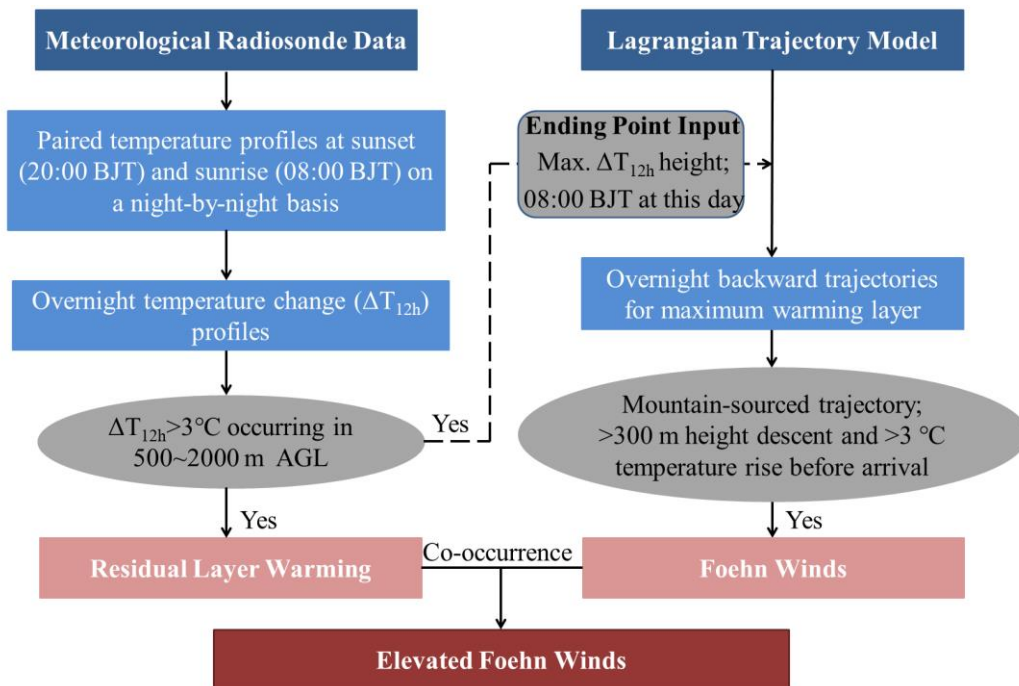
114 To validate the lidar O₃ observations, we compared the lidar-derived O₃ concentration at 300 m height (the lowest
115 reliable altitude above the instrument’s blind zone) with surface measurements. As no surface O₃ data were
116 available at the GXT site, we used measurements from the nearest air quality monitoring station (~2 km away). The
117 validation results demonstrated a strong correlation between the lidar-based and surface-based O₃ concentrations
118 ($R^2 = 0.69$ at GXT and $R^2 = 0.56$ at SDZ), confirming the reliability of the O₃ lidar data (Fig. S1). To construct

119 complete vertical profiles for calculating O₃ transport flux, we used linear interpolation between the surface O₃
 120 measurement and the validated lidar observation at 300 m to fill the blind zone. A similar procedure was applied to
 121 patch the blind zone (below 150 m) of the radar wind profiler data, where winds were interpolated between the
 122 surface wind observation and the lowest valid radar measurement at 150 m.

123

124 | 2.2. Identification of elevated foehn

125 To date, no established method exists for identifying elevated foehn. For the purpose of climatological evaluation,
 126 we develop a framework (Fig. 2) to identify elevated foehn events based on the combination of meteorological
 127 radiosonde data and a Lagrangian trajectory model. First, we calculated overnight temperature change (ΔT_{12h})
 128 profiles by subtracting the radiosonde temperature profiles at 20:00 BJT (sunset) from the profiles at 08:00 BJT the
 129 following day (sunrise) on a night-by-night basis (i.e., $\Delta T_{12h}=T_{08}-T_{20}$). A residual layer warming event was
 130 identified when $\Delta T_{12h}>3^{\circ}\text{C}$ occurred within 500-2000 m AGL layer. This threshold is also commonly used to
 131 identify ground-based foehn elsewhere (Kirchgaessner et al., 2021; Steinhoff et al., 2014). Finally, we examined the
 132 backward trajectory properties (including geographic origin, height change, and temperature change) of the air
 133 mass at the identified maximum warming height (i.e., the height of maximum ΔT_{12h}) using a Lagrangian trajectory
 134 model (Miltenberger et al., 2016). If the 12-h backward trajectory originated from the mountains (azimuth of 250–
 135 360° or 0–45°, following Li et al. (2025)), and if the trajectory descended more than 300 m accompanied by a
 136 temperature increase exceeding 3 °C before arriving in Beijing, we attribute the identified warming case to an
 137 elevated foehn event.



138

139 **Figure 2.** Flowchart for identifying elevated foehn based on the combination of meteorological radiosonde data and
 140 a Lagrangian trajectory model.

141

142 2.3. Supporting calculations and model simulations

143 The boundary layer structure during a diurnal cycle can be classified into three regimes: convective boundary
 144 layer (CBL), stable boundary layer (SBL), and residual layer (RL) (Stull, 1988). We determined the boundary layer
 145 height based on high-resolution radiosonde profiles from the GXT station. Following Liu and Liang (2010), the
 146 height of the CBL (CBLH, at 14:00 BJT) was determined at the base of the overlying temperature inversion

147 capping the convective thermals. The height of the SBL (SBLH, at 20:00 and 08:00 BJT) was determined at the top
148 of the underlying temperature inversion, where turbulence nearly ceases. At the morning transition (08:00 BJT),
149 emerging solar radiation gradually erodes the near-surface part of the SBL; thus, the SBLH at this time was
150 determined at the top of the residual underlying temperature inversion. The RL is disconnected from the ground by
151 the underlying SBL but retains the atmospheric state of the former CBL. Its height (RLH) was therefore determined
152 at the base of the overlying temperature inversion at the evening or morning transition (20:00 and 08:00 BJT). For
153 temperature profiles showing no significant overlying inversion, the CHLH and RLH were determined using a
154 multi-variable integrated method proposed by Wang and Wang (2014).

155
156 To analyze O₃ transport in Beijing, we calculated the O₃ transport flux (TF) using collocated wind and O₃ profiles
157 from the GXT and SDZ sites. The transport flux (TF, mg m⁻² s⁻¹), representing the mass flow per unit
158 cross-sectional area per unit time, is determined by the wind speed and the O₃ concentration. The TF at a certain
159 height and direction is calculated as follow:

$$TF = C \times WS \times \cos \left[(WD - B) \times \frac{\pi}{180} \right]$$

160 where C represents the O₃ concentration (unit: μg m⁻³), WS denotes the horizontal wind speed (unit: m s⁻¹), WD
161 denotes the horizontal wind direction and B is the azimuth from the start station to the end station. In this study, we
162 calculated O₃ transport flux in the direction from GXT to SDZ. Therefore, positive TF indicates northeastward
163 transport, and negative TF indicates southwestward transport.

164
165 We used the Hybrid Single-Particle Lagrangian Integrated Trajectory (HYSPPLIT) model (Stein et al., 2015) to
166 trace the origin and history of the air masses associated with the maximum residual layer warming in Beijing. In
167 addition to HYSPPLIT, we employed the Weather Research and Forecasting model with Chemistry (WRF-Chem,
168 version 4.2.1) to simulate O₃ concentrations and meteorological fields. The WRF-Chem model accounts for key
169 atmospheric processes, including emissions, deposition, advection, diffusion, gas-phase chemistry, and aerosol
170 chemistry (Grell et al., 2005). Our simulation domain encompassed most of China, centered at (105.5 °E, 37.5 °N),
171 with a horizontal grid spacing of 9 km. The meteorological initial and boundary conditions were derived from the
172 National Centers for Environmental Prediction (NCEP) Final Operational Global Analysis data. For emissions, we
173 utilized the Model of Emissions of Gases and Aerosols from Nature (MEGAN) (Guenther et al., 2006) and the
174 Multi-resolution Emission Inventory for China (MEIC) (Zhang et al., 2009), with the latter updated to a 0.1 ° × 0.1 °
175 resolution for 2019 (MEIC-2019; <http://www.meicmodel.org>). The detailed model configuration follows Xu et al.
176 (2024). The WRF-Chem simulation demonstrated a reasonable agreement with observed surface O₃ concentrations
177 during the studied pollution episode ($R^2 = 0.51$ at GXT and $R^2 = 0.44$ at SDZ; Fig. S2).

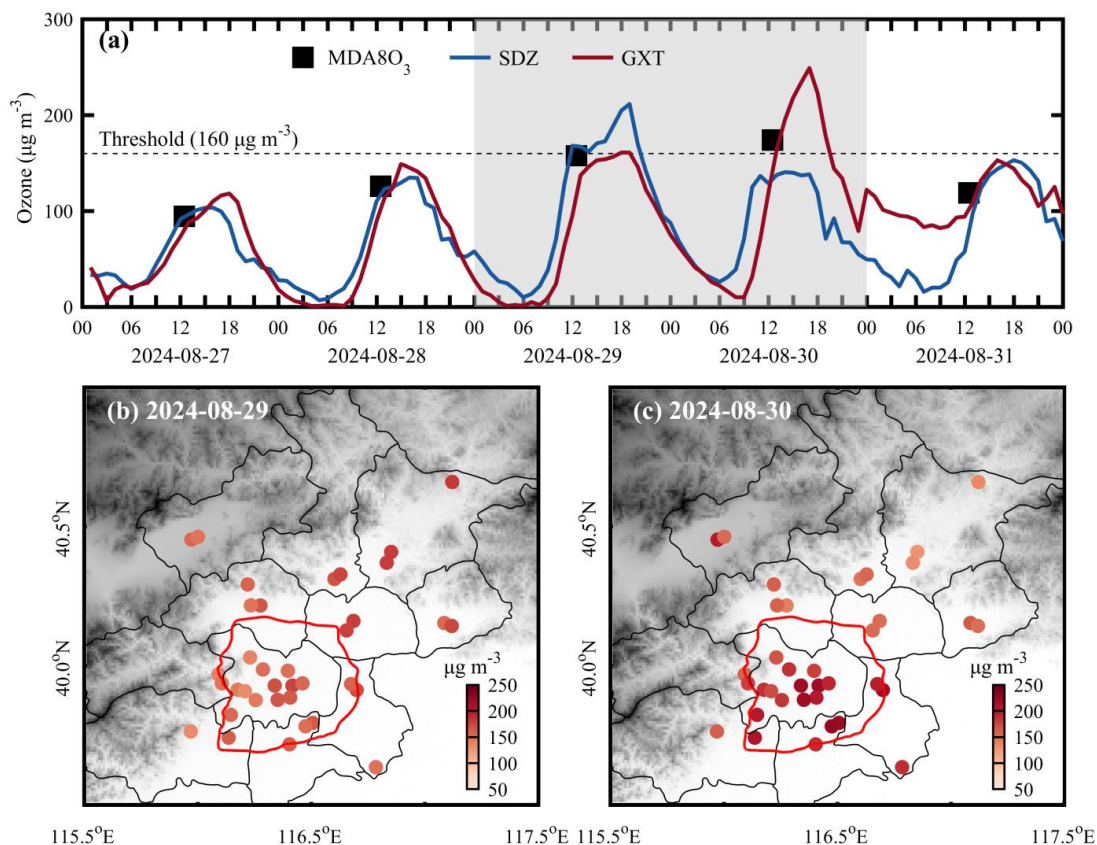
178 179 **3. Results**

180 **3.1. Case study**

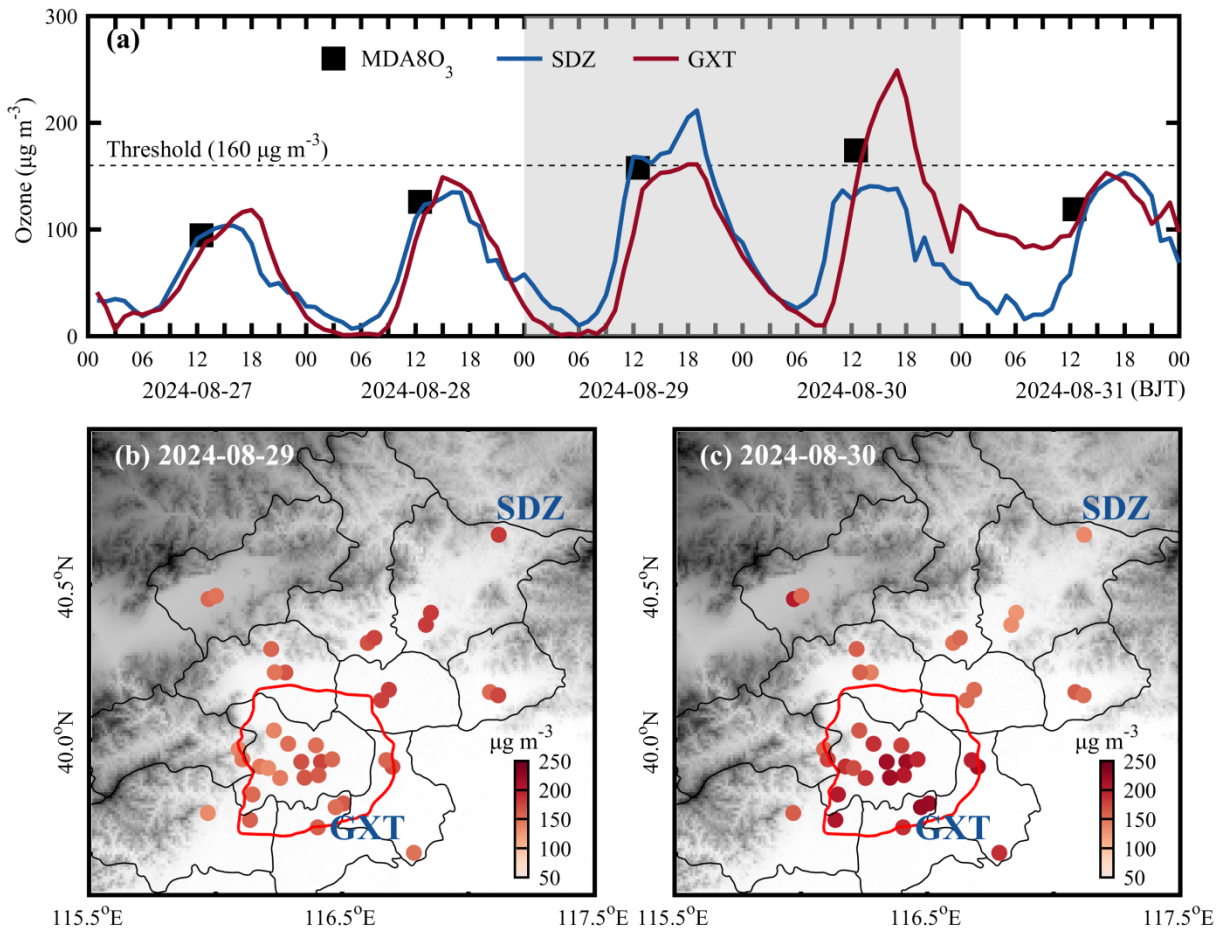
181 **3.1.1. Overview of the O₃ pollution episode**

182 Following heavy rainfall on 26 August 2024, Beijing experienced consecutive sunny days until light rain
183 resumed on 31 August. The persistent sunny weather established favorable meteorological background for
184 photochemical O₃ production. Consequently, surface O₃ concentrations in Beijing exhibited a daily increasing trend
185 from 27 to 30 August. On the final two days (29 and 30 August), the city-averaged daily maximum 8-hour average
186 O₃ (MDA8O₃) concentrations approached or exceeded China's ambient air quality standard threshold of 160 μg m⁻³,
187 peaking at 174 μg m⁻³ on 30 August (Fig. 3a). A notable feature of these two polluted days was the stark contrast in
188 the spatial distribution of O₃ concentrations. On 29 August, the spatial pattern showed a positive O₃ gradient

189 extending northeastward, which was reversed on 30 August (Fig. 3b, c). This contrast was exemplified by the
 190 station observations: SDZ recorded its peak O₃ concentration (212 μg m⁻³ at 18:00 BJT) on 29 August, significantly
 191 higher than the concurrent value at GXT (161 μg m⁻³). Conversely, GXT observed its maximum O₃ level (249 μg
 192 m⁻³ at 16:00 BJT) on 30 August, far exceeding the measurement at SDZ (138 μg m⁻³; Fig. 3a). These contrasting
 193 spatial patterns seem to represent two typical O₃ pollution scenarios in Beijing: an urban plume transport pattern
 194 and an urban pollution accumulation pattern, as previously reported by Zong et al. (2023). The key question is what
 195 mechanism drove the rapid intensification of O₃ pollution and the reversal of its spatial pattern over the two
 196 consecutive days.



197



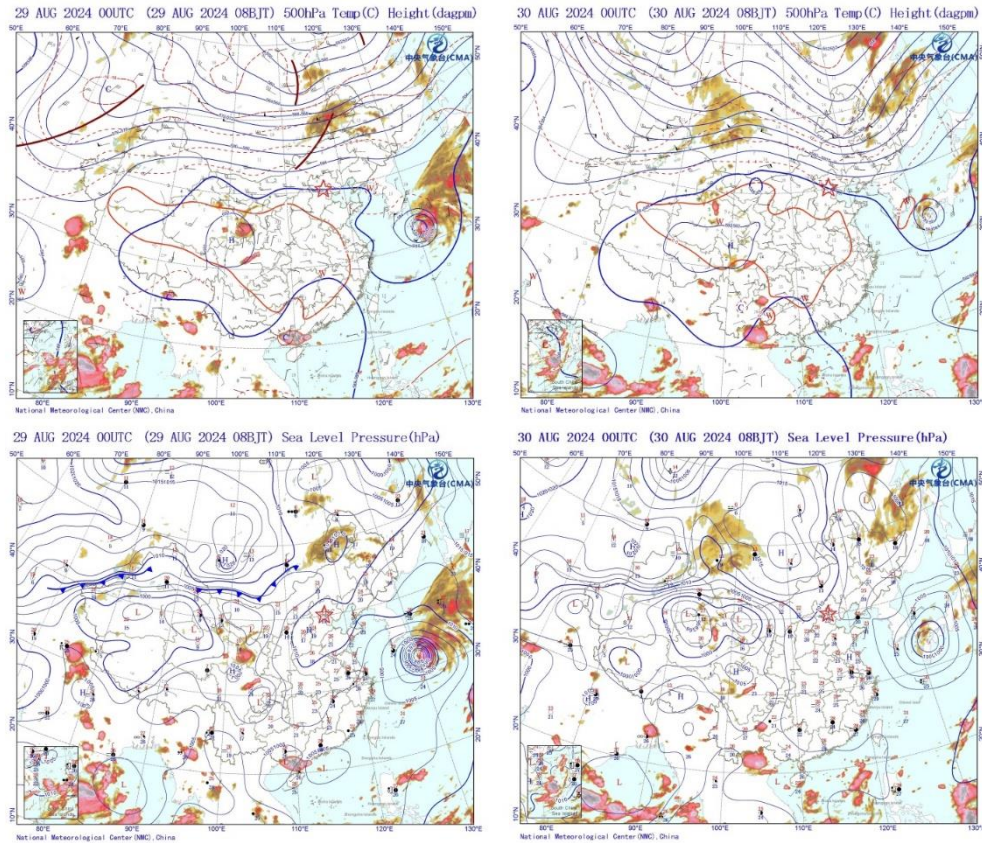
198

199 **Figure 3.** (a) Time series of surface ozone concentrations at the GXT and SDZ stations from 27 to 31 August 2024;
 200 Spatial distribution of maximum 8-h O_3 concentrations over Beijing on (b) 29 and (c) 30 August. In (a), black
 201 squares represent the city-averaged MDA8O_3 concentrations; gray shading denotes the two polluted days (29 and
 202 30 August 2024).

203

204 3.1.2. Meteorological attribution to elevated foehn

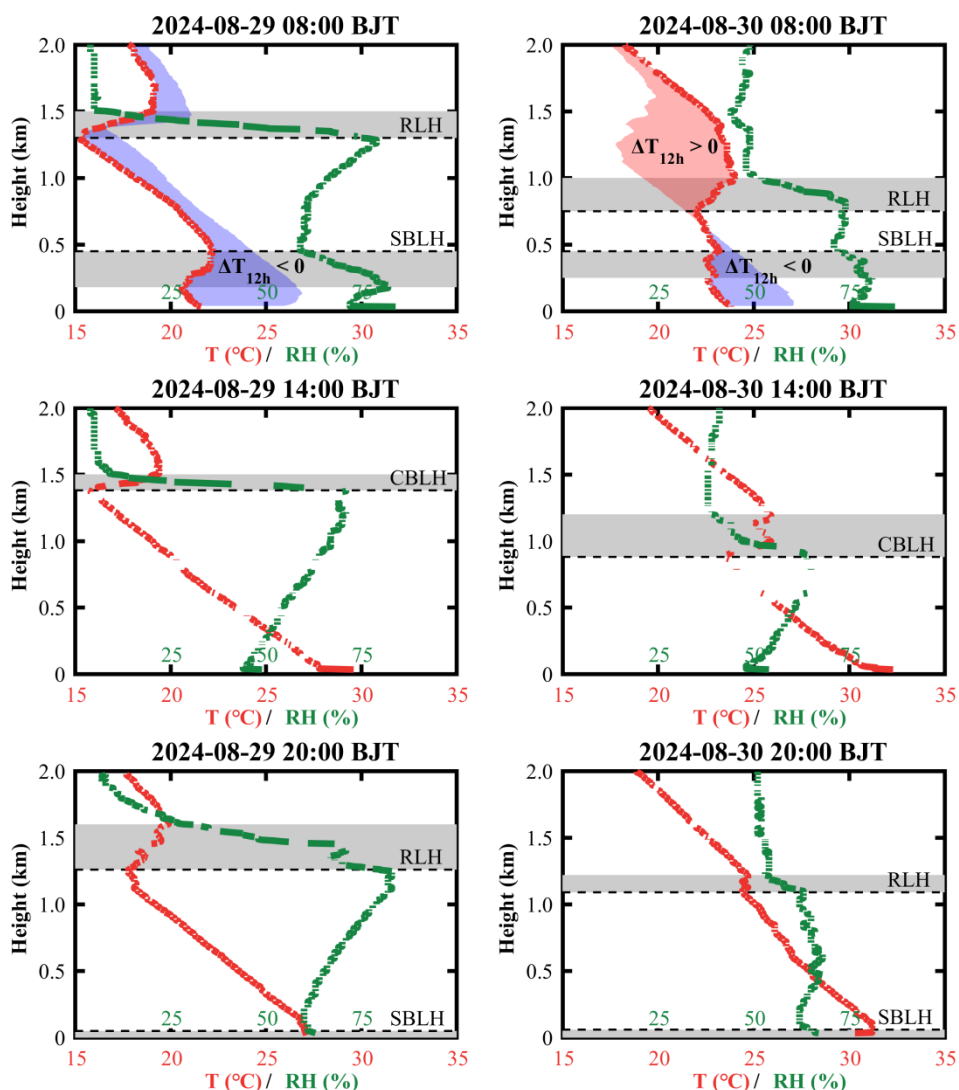
205 The weather charts at 08:00 BJT on 29 and 30 August are presented in Fig. 4. A subtropical high prevailed in the
 206 upper atmosphere over the central and eastern China, while a typhoon was active over the western Pacific Ocean
 207 south of Japan. The coexistence of these two synoptic systems induced widespread clear skies over the eastern
 208 China, a condition highly conducive to photochemical O_3 production (Ouyang et al., 2022; Shu et al., 2016). In the
 209 lower atmosphere, the synoptic patterns differed between the two days. On 29 August, the North China Plain (NCP)
 210 was under the influence of a weak high-pressure system. By 30 August, another high-pressure system (a cold front)
 211 had intruded into the northwestern NCP from the Mongolian Plateau, creating a strong pressure gradient
 212 perpendicular to the Taihang Mountains. Traditionally, cold fronts are known to have a significant clearance effect
 213 on air pollutants (Zhang et al., 2021). However, in this case, the cold front led to an unexpected O_3 increase in
 214 Beijing on 30 August. So, what underlying mechanism was responsible for this phenomenon?



215
 216 **Figure 4.** Weather charts at 500 hPa and sea-level pressure over the East Asia at 08:00 BJT on 29 and 30 August,
 217 2024. Shaded areas denote the cloud cover. The location of Beijing is marked by a red star.

218
 219 To address the question above, we examined the radiosonde profiles and derived boundary layer heights at the
 220 GXT station (Fig. 5). The results indicate that the CBLH and RLH on 30 August (750, 880, and 1090 m at 08:00,
 221 14:00, and 20:00 BJT, respectively) were significantly lower than those on 29 August (1300, 1380, and 1260 m at
 222 the same times), despite the SBLH showing no significant difference. The CBLH defines the available volume that
 223 the pollutants emitted/produced near the surface can occupy, directly affecting their surface concentration and air
 224 quality (Tang et al., 2016). Evidently, the significant decline in CBLH contributes to the surface O₃ enhancements
 225 in urban Beijing on 30 August. Notably, the two-day CBLH difference originated from a sharp drop (more than 500
 226 m) in RLH between 20:00 BJT on 29 August and 08:00 BJT on 30 August. Comparing radiosonde profiles from
 227 these two time points revealed abnormal drying and warming in the residual layer, with a maximum temperature
 228 increase of up to 5.8 °C at 1250 m, contrasting sharply with the normal cooling observed the previous night. The
 229 base height of this warming layer coincided precisely with the RLH observed at 08:00 BJT on 30 August,
 230 indicating that the warming process was responsible for the overnight RLH drop and thereby contributed to the
 231 subsequent daytime O₃ pollution exacerbation. Furthermore, the nocturnal residual layer warming inevitably
 232 contributes to higher daytime air temperatures. As observed, the afternoon boundary layer temperature on 30
 233 August showed a significant increase compared to the previous afternoon, and this higher temperature further
 234 promotes photochemical O₃ production by accelerating photochemical reaction rates and enhancing emissions of
 235 volatile organic compounds and soil nitric oxide (Gu et al., 2020; Wu et al., 2024). That is to say, in addition to
 236 promoting daytime O₃ accumulation by reducing the boundary layer height, residual layer warming also enhances
 237 daytime the photochemical O₃ production. Moreover, these changes in boundary layer thermal properties can
 238 facilitate O₃ accumulation by lowering the O₃ loss. For instance, the lowered CBLH can reduce transport of PAN

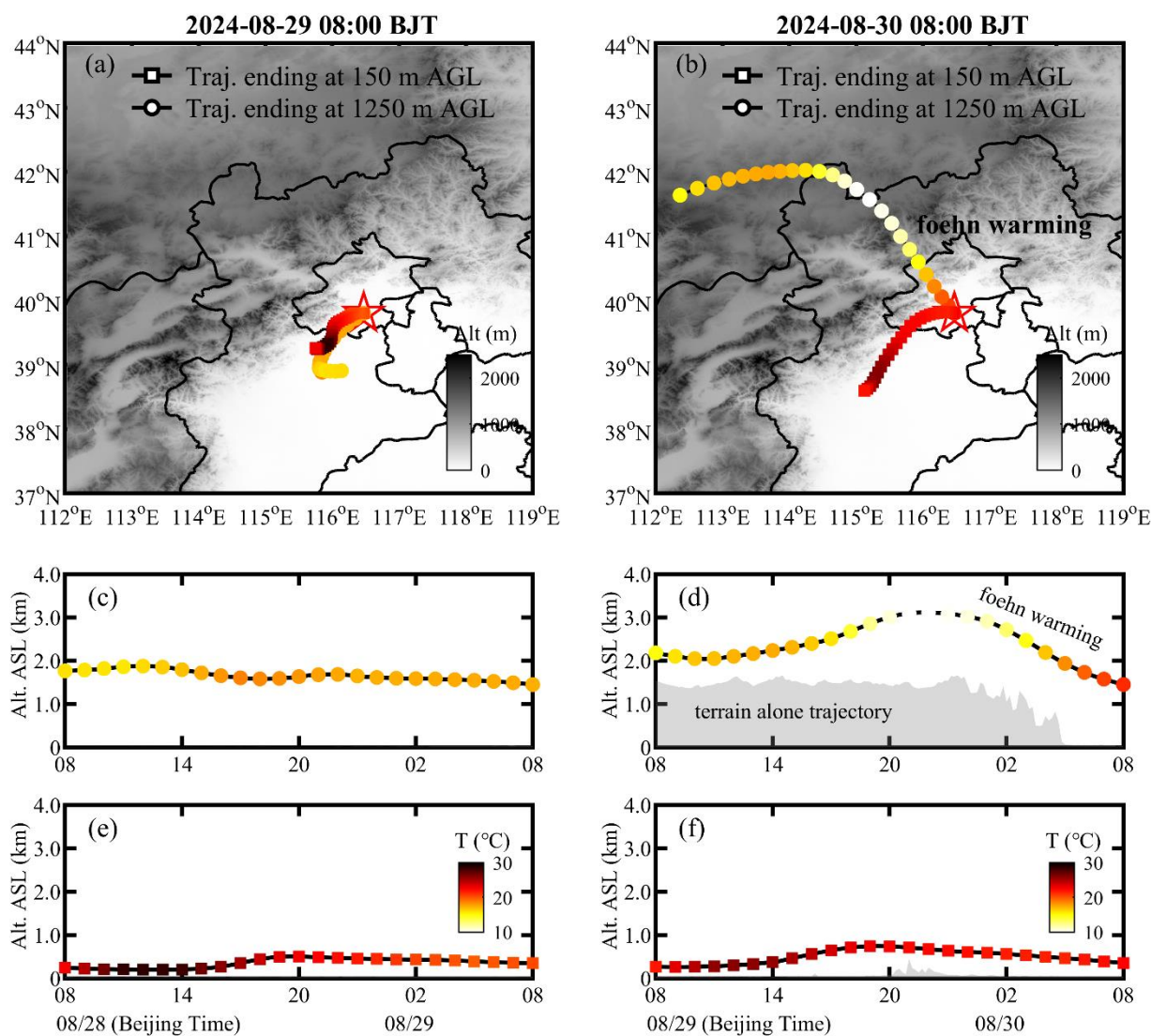
239 (peroxyacetyl nitrate, a NO_x reservoir in the upper atmosphere) into urban Beijing (a NO_x-saturated zone), which
 240 may suppress O₃ loss from NO titration and independently contribute to the observed O₃ increases (Flowerday and
 241 Hansen, 2026). The remaining question is: what caused the abnormal warming of the nocturnal residual layer under
 242 the background of a cold front intrusion?



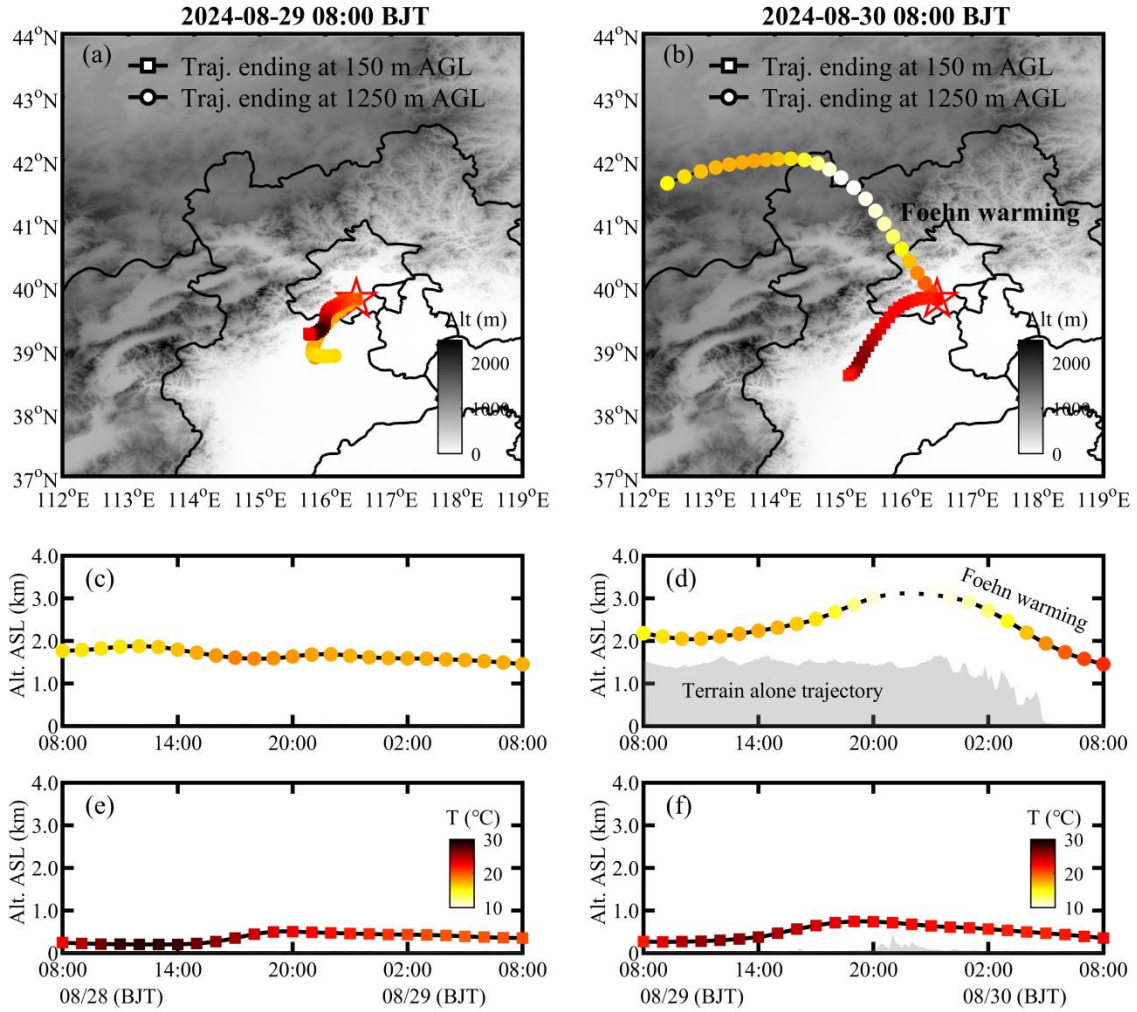
243 **Figure 5.** Radiosonde-based temperature (T, red lines) and relative humidity (RH, green lines) profiles at the GXT
 244 station. Gray shaded areas represent the heights of temperature inversion layers. Dashed lines denote the afternoon
 245 convective boundary layer height (CBLH), and dot lines denote the nocturnal stable boundary layer height (SBLH).
 246 Colorful shaded areas highlight the overnight temperature changes, with increase marked in red and decrease in
 247 blue. Note: at 08:00 BJT (morning transition), emerging solar radiation collapses the near-surface SBL; thus, the
 248 SBLH at this time is determined at the top of the residual underlying temperature inversion.
 249

250
 251 Using the HYSPLIT model, we traced the 24-hour origin and characteristics of the air mass at the overnight
 252 maximum warming height (1250 m) observed at 08:00 BJT on 30 August (Fig. 6b and d). For comparison, we also
 253 calculated backward trajectories for the near-surface (150 m) airflow at the same time (Fig. 6b and f), as well as
 254 airflows at the same heights and time on the previous day (Fig. 6a, c, and e). The results show that the airflows at
 255 1250 m and 150 m on 29 August, as well as at 150 m on 30 August, all originated from the southern NCP region
 256 with no significant change in trajectory height. In contrast, the air mass at the maximum warming height on 30

257 August originated from the Mongolian Plateau. It moved eastward to the northern side of the Yanshan Mountains,
 258 turned southeastward to cross the mountains, and finally arrived in Beijing. During this transport, the airflow first
 259 ascended about 1000 m and then descended about 1500 m, accompanied by a temperature change of cooling (7.6°C)
 260 followed by warming (11.4°C). These changes in trajectory height and temperature exhibit very pronounced foehn
 261 warming characteristics (Elvidge and Renfrew, 2016). Previous studies have reported several cases of shallow
 262 foehn-induced nocturnal surface warming in Beijing (Li et al., 2026; Luo et al., 2020). Our case differs significantly
 263 because it involves elevated air masses and shows no warming in the surface layer. To confirm this, we examined
 264 hourly temperature variations from 20:00 BJT on 29 August to 08:00 BJT on 30 August at 20 surface
 265 meteorological stations in Beijing (Fig. S3), as well as at 15 levels on a 325 m high meteorological tower (Fig. S4).
 266 The results revealed that, except for the high-altitude Foyeding station (1224.9 m), no temperature surges
 267 ($\Delta T_{1h} > 1^\circ\text{C}$) were observed before sunrise (around 06:00 BJT) at the other stations. This implies no detectable
 268 foehn warming signature from standard mountain-leeside surface observations (Li et al., 2025), despite the strong
 269 foehn signature in the residual layer. Therefore, we identify this case as the first observation of a novel type of
 270 foehn phenomenon in Beijing: elevated foehn in the residual layer.



271



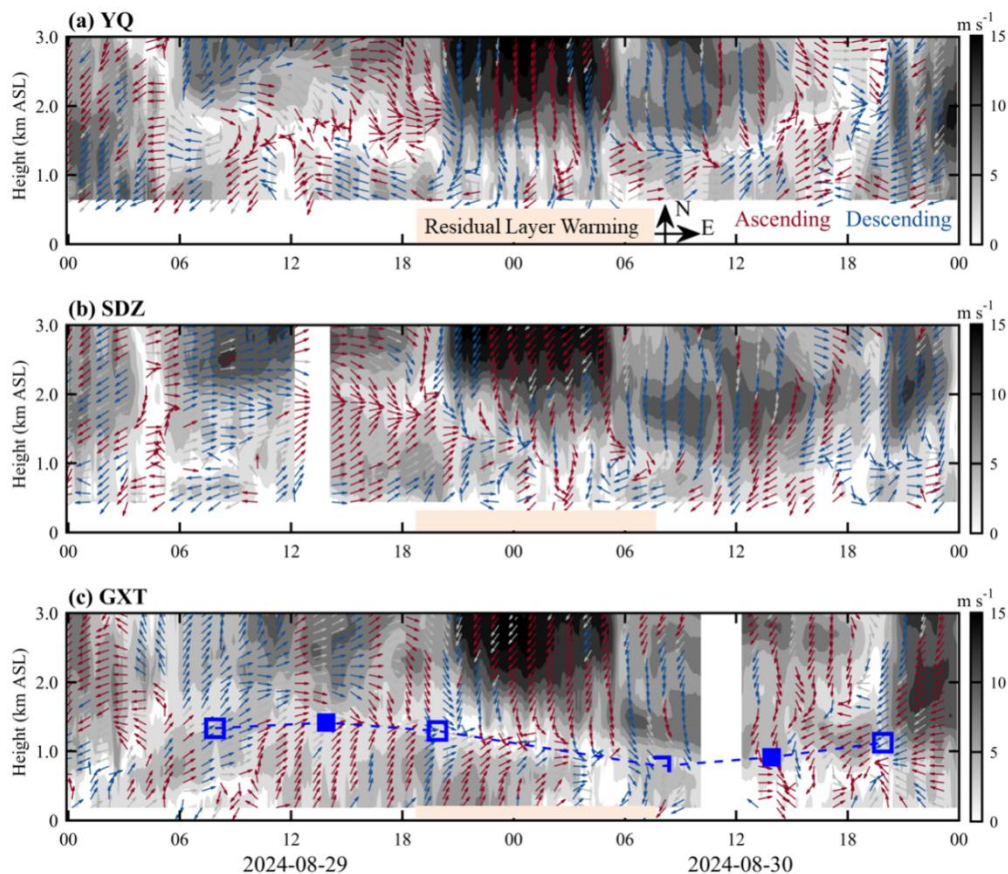
272

273 **Figure 6.** 24-h backward trajectories ending at 150 m (squares) and 1250 m (dots) above ground level (AGL) over
 274 the GXT station, at 08:00 BJT of (a) 29 and (b) 30 August. The 1250 m level corresponds to the maximum
 275 overnight warming height at 08:00 BJT on 30 August (see Fig. 5). Panels (c-f) show the height and temperature
 276 changes of 24-h backward trajectories at 150 and 1250 m. All temperature changes share the same colorbar,
 277 including those in (a) and (b).

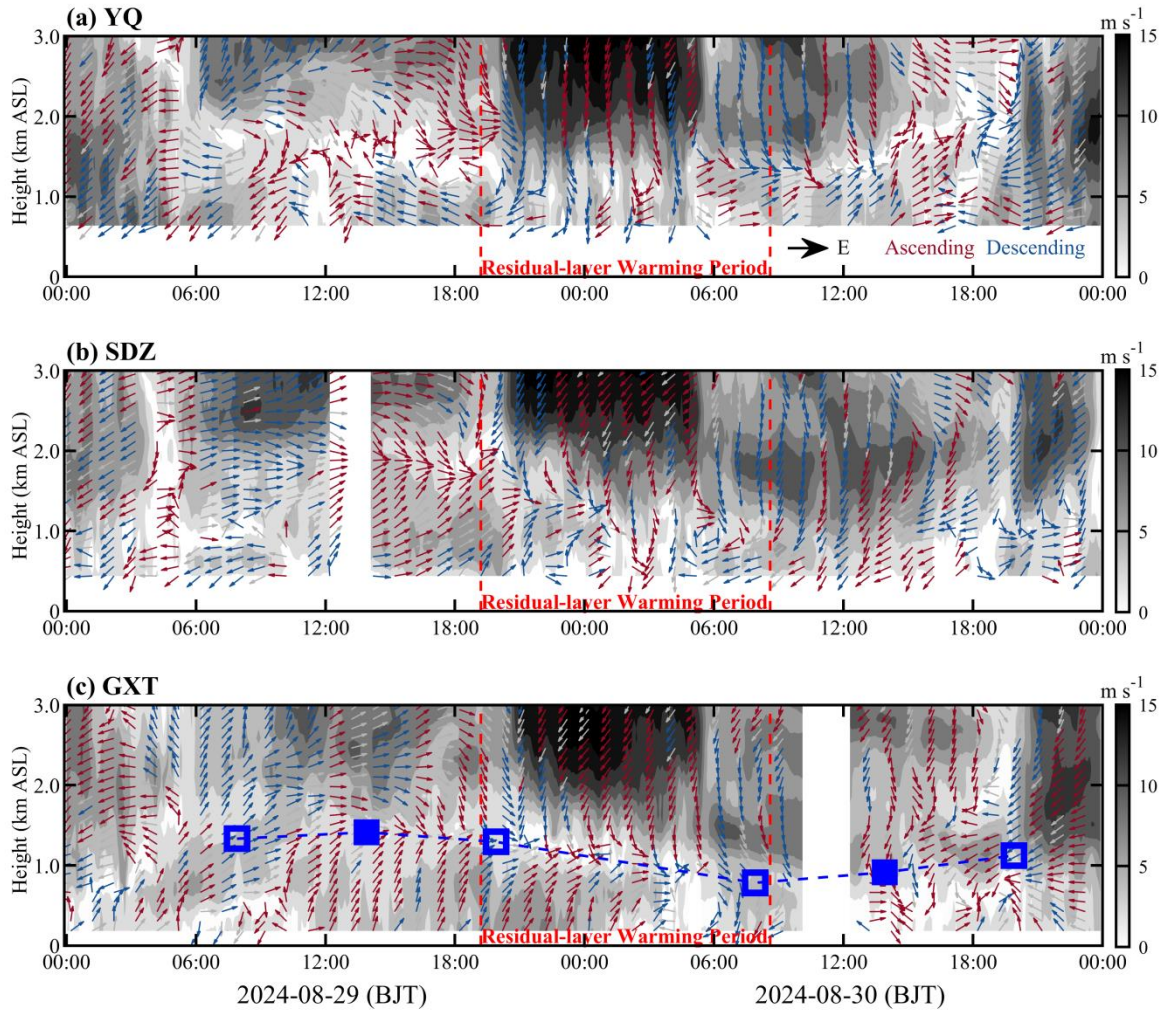
278

279 To illustrate the dynamical conditions during the elevated foehn-induced residual layer warming, Figure 7 presents
 280 the radar wind profiles at the YQ, SDZ, and GXT stations from 29 to 30 August. Prior to the warming, southerly
 281 winds prevailed in the boundary layer (southwesterly at SDZ and GXT; southeasterly at YQ), while lower
 282 free-tropospheric winds gradually shifted from southwesterly to northwesterly. After sunset on 29 August, the cold
 283 front intrusion induced strong northeasterly winds in the lower free troposphere at all stations. These northeasterly
 284 winds aloft first descended into the boundary layer at YQ, followed by SDZ. In contrast, GXT maintained
 285 southwesterly boundary-layer winds until later in the night, forming a distinct northwesterly wind shear zone aloft.
 286 During this process, the height of the northwesterly wind shear corresponded well with the sounding-derived RLH
 287 at GXT, and the northwesterly winds matched the HYSPLIT backward trajectories ending at GXT (Fig. 6b).
 288 Combining the HYSPLIT results, these features strongly support the mechanism of an elevated northwesterly foehn
 289 during the residual layer warming period. The elevated foehn appears to have occurred within a shallow wind shear
 290 zone, similar to the elevated foehn scenario reported in winter Urumqi by Li et al. (2015). After the residual layer
 291 warming, northeasterlies prevailed in the boundary layer at SDZ and southwesterlies at YQ, whereas GXT showed

292 highly variable winds with weak speeds—likely due to convergence between the emerging northwesterly foehn and
293 the prevailing southwesterly flows. This weak-wind stagnant condition suppressed the horizontal dispersion of air
294 pollutants. Operating in conjunction with the inhibited vertical dispersion (from a lower boundary layer height) and
295 accelerated photochemical production (due to higher temperatures), this post-foehn convergent stagnation represent
296 a third contributing factor to the severe daytime O₃ pollution observed in urban Beijing on 30 August.



297



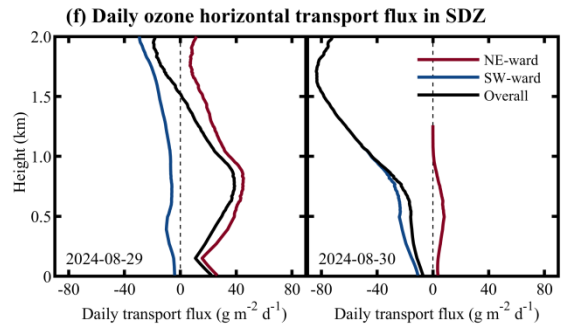
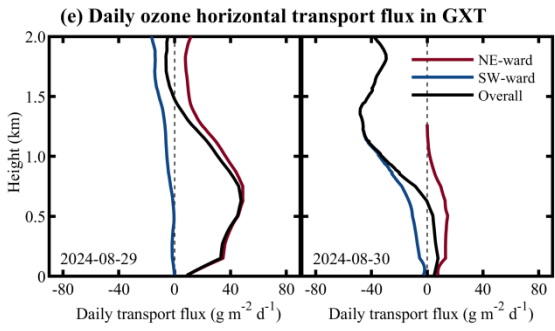
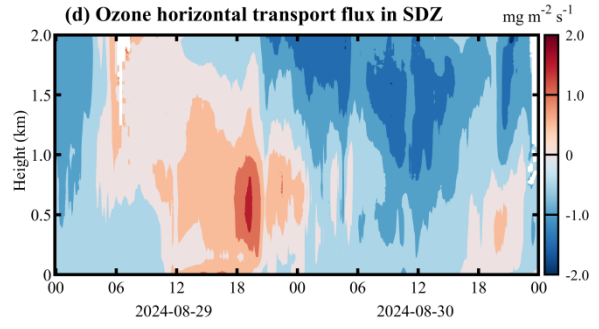
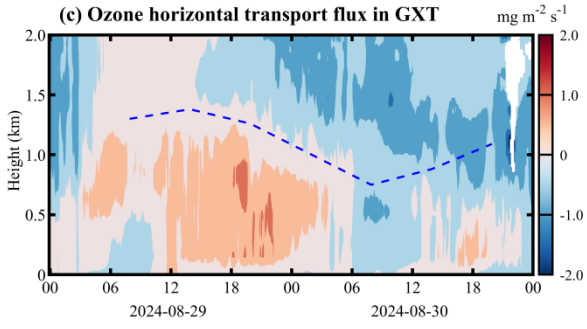
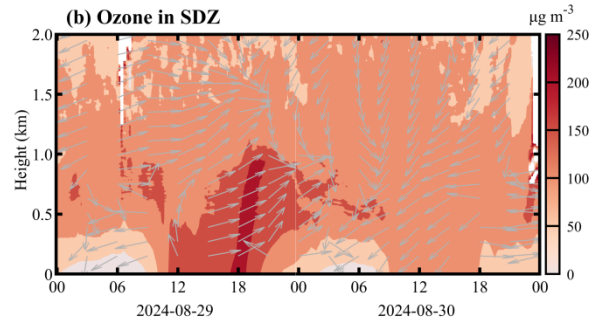
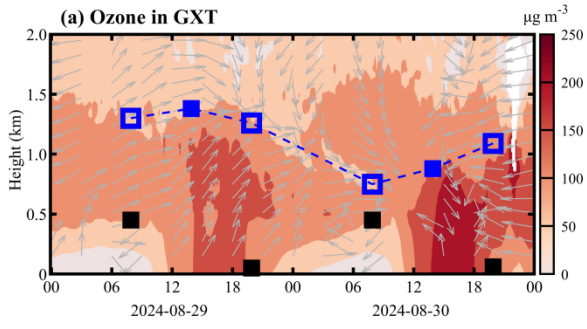
298

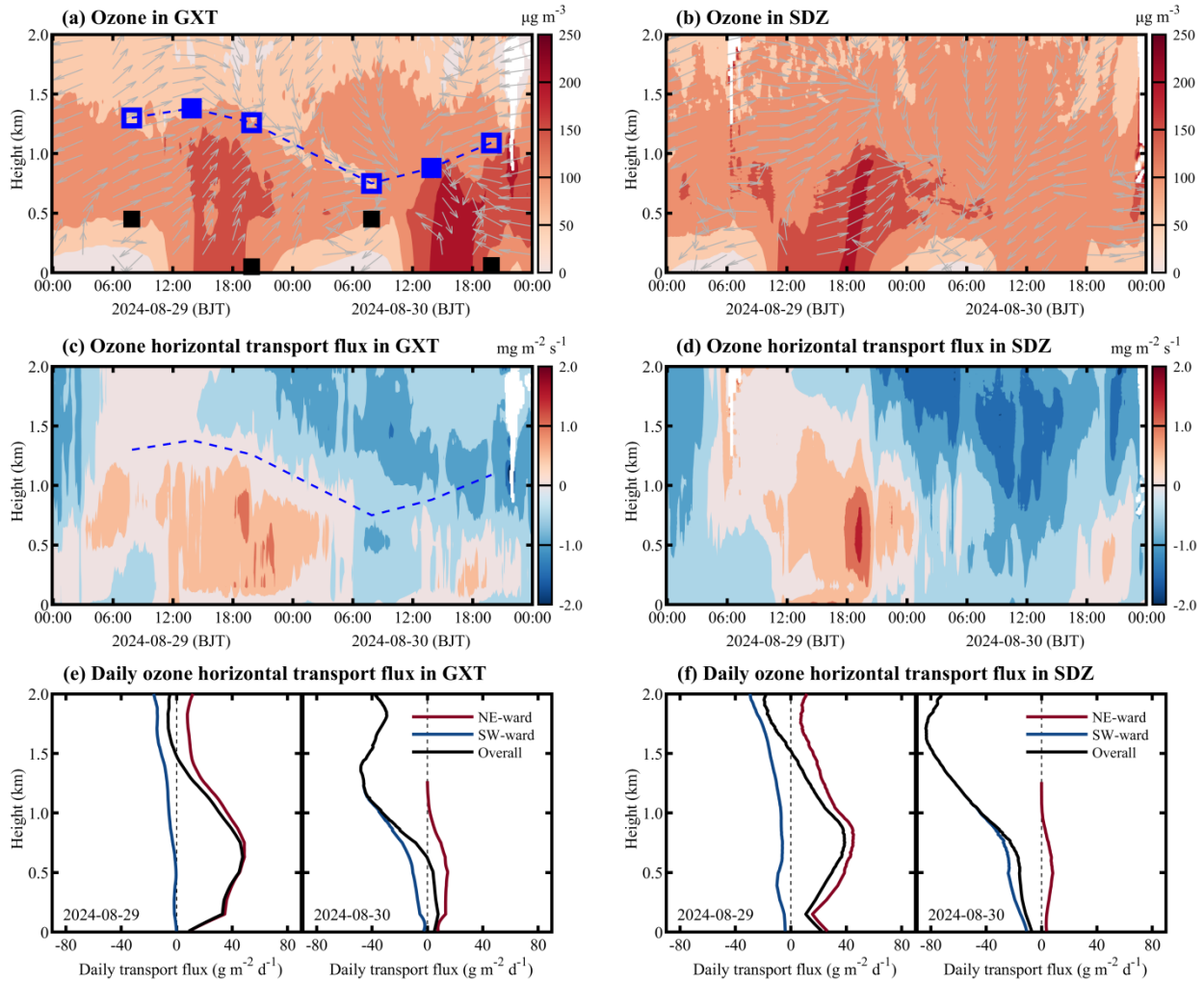
299 **Figure 7.** Radar-based wind profiles at the (a) YQ, (b) SDZ, and (c) GXT stations before, during, and after the
 300 elevated foehn-induced residual layer warming. Shaded areas represent horizontal wind speed; arrows denote
 301 horizontal wind direction (red indicates ascending motion, blue indicated descending motion). In (c), blue squares
 302 denote the convective boundary layer height (solid) or residual layer height (hollow); blue dashed line indicates the
 303 evolution of the convective boundary layer and residual layer heights.

304

305 3.1.3. Three-dimensional evolution of O₃ before, during, and after elevated foehn

306 The coordinated O₃ lidar observations at the urban (GXT) and rural (SDZ) stations provided a unique
 307 opportunity to elucidate the three-dimensional evolution of boundary-layer O₃ in response to elevated foehn. By
 308 integrating data from meteorological radiosondes and radar wind profilers, we investigated how sudden changes in
 309 boundary layer thermal and dynamical structure induced by elevated foehn affected O₃ evolution and quantified the
 310 differences in boundary layer O₃ transport fluxes between the pre- and post-foehn days (Fig. 8).





312

313 **Figure 8.** Vertical O_3 concentrations, wind direction, and O_3 transport flux at the GXT and SDZ stations. In (a),
 314 squares denote the boundary layer heights determined from radiosonde profiles (black for SBLH, blue for
 315 CBLH/RLH). The blue dashed line in (a) and (c) indicates the evolution of CBL and RL heights. In (c) and (d),
 316 positive (negative) horizontal transport flux indicates northeastward (southwestward) transport in the direction from
 317 GXT to SDZ. Panels (e) and (f) show the daily integrated O_3 transport flux at the GXT and SDZ stations on 29 and
 318 30 August, respectively.

319

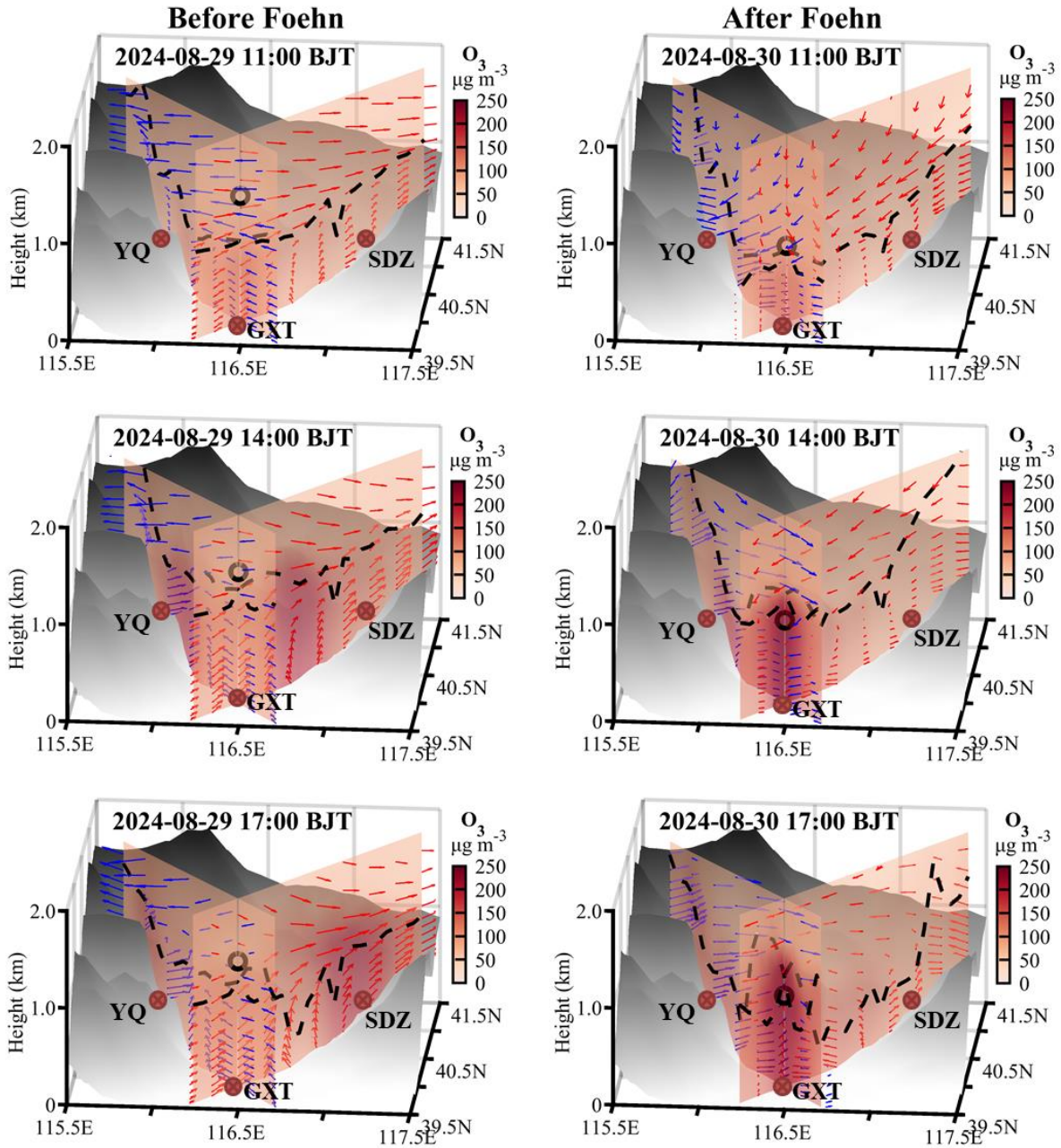
320 As shown in Fig. 8a, the boundary layer thermal structure critically shaped O_3 vertical distribution in urban
 321 Beijing: a steep gradient in the SBL, an O_3 reservoir in the RL, and relatively uniform mixing in the CBL. The
 322 elevated foehn-induced residual layer warming on the night of 29–30 August led to a significant reduction in the
 323 boundary layer height on 30 August, substantially compressing the vertical space for daytime O_3 mixing. Combined
 324 with enhanced photochemical O_3 production (due to higher temperatures) and weakened horizontal dispersion (due
 325 to lower post-foehn wind speeds,) these factors collectively contributed to a marked increase in afternoon boundary
 326 layer O_3 concentrations in urban Beijing on 30 August ($200\text{--}250 \mu\text{g m}^{-3}$) compared to the previous day ($\sim 150 \mu\text{g}$
 327 m^{-3}). We also observed that the elevated foehn was accompanied by downward transport of free-tropospheric O_3
 328 (Fig. 8a). However, due to the presence of a strong capping inversion acting as a transport barrier (Fig. 5), this
 329 descending free-tropospheric O_3 was unlikely to have significantly intruded into the boundary layer.

330

331 The urban-rural coordinated lidar observations clearly reveal a dynamically driven shift in spatial heterogeneity
332 before and after the elevated foehn. On 29 August (pre-foehn), prevailing southwesterly flows facilitated the
333 northeastward transport of the urban O₃ plume. The lidars recorded higher O₃ concentrations at the downwind rural
334 SDZ station than at the urban GXT station (Fig. 8a and b). The peak O₃ occurrence at SDZ was delayed by 1–3
335 hours relative to GXT, consistent with advective transport. The calculated horizontal O₃ transport flux was
336 predominantly northeastward in the boundary layer at both stations throughout the day, with stronger fluxes in the
337 upper boundary layer. The instantaneous maximum flux at SDZ exceeded 2.0 mg m⁻³ s⁻¹, significantly higher than
338 at GXT (Fig. 8c and d). In stark contrast, the post-foehn convergence stagnation on 30 August suppressed advective
339 transport and promoted local O₃ accumulation in urban Beijing. Consequently, afternoon boundary layer O₃
340 concentrations at GXT reached notably high levels (200–250 µg m⁻³), while concentrations at SDZ dropped to low
341 values (~100 µg m⁻³). Despite this spatial contrast, the boundary layer O₃ transport flux at both stations was
342 markedly low compared to the previous day (Fig. 8c, d, e, and f), underscoring a shift in the dominant pollution
343 mechanism from urban plume transport to urban pollution accumulation.

344

345 We examined the WRF-Chem output to gain further insight into the vertical O₃ structure over Beijing before and
346 after the elevated foehn. As shown in Fig. 9, although the WRF-Chem model exhibited some deviations in
347 simulating the boundary layer height, it successfully reproduced the pre-foehn northeastward transport of the urban
348 O₃ plume on 29 August, as well as the post-foehn stagnation-driven local O₃ accumulation in the urban Beijing on
349 30 August. On 29 August, the O₃ pollution initially built up in the urban area (e.g., near GXT) by 11:00 BJT. By
350 14:00 BJT, the high-O₃ zone had shifted to the northern suburbs, and by 17:00 BJT, it had been transported to the
351 rural areas in the northeast (e.g., near SDZ). In contrast, on 30 August, the relatively higher O₃ concentrations over
352 Beijing were consistently confined in the urban area, with no significant spatial shift. These simulation results
353 aligned well with the lidar observations. Furthermore, the WRF-Chem model reproduced the vertical wind patterns
354 observed at GXT, SDZ, and YQ (Fig. 7), thereby better illustrating the vertical structure of the foehn flow during its
355 decaying stage on 30 August via wind cross-sections. The foehn simulations show that while the near-surface
356 component—shallow foehn—was blocked by prevailing southerly winds within the boundary layer, leading to
357 convergence and airflow stagnation over urban Beijing, its upper-layer branch—elevated foehn—passed directly
358 over the urban area unimpeded, resulting in persistent warming that suppressed the daytime convective boundary
359 layer development until the foehn decayed around 14:00 BJT. These features are evident in both the GXT-YQ
360 cross-section (parallel to the elevated northwesterly foehn) and the GXT-SDZ cross-section (perpendicular to the
361 elevated northwesterly foehn). The configuration of an unimpeded elevated foehn and a blocked shallow foehn
362 effectively explains the accumulation of higher O₃ concentrations in the urban boundary layer of Beijing on 30
363 August.



364

365 **Figure 9.** Cross-sections of simulated O_3 concentrations along the line across the GXT and SDZ stations and the
 366 line across GXT and YQ stations on 29 and 30 August. Dashed black lines denote the simulated boundary layer
 367 height, and arrows show the composite of simulated horizontal wind speed ($m s^{-1}$) and vertical wind speed ($\times 10 m$
 368 s^{-1}) in the GXT-SDZ (red arrows) and GXT-YQ (blue arrows) cross-sections. Only horizontal wind speed in the
 369 direction along the individual cross-sections is included. The black dots denote the boundary layer height observed
 370 at GXT and the height at 14:00 BJT is the observational value and these at 11:00 and 17:00 BJT are interpolated
 371 from two adjacent radiosonde observations.

372

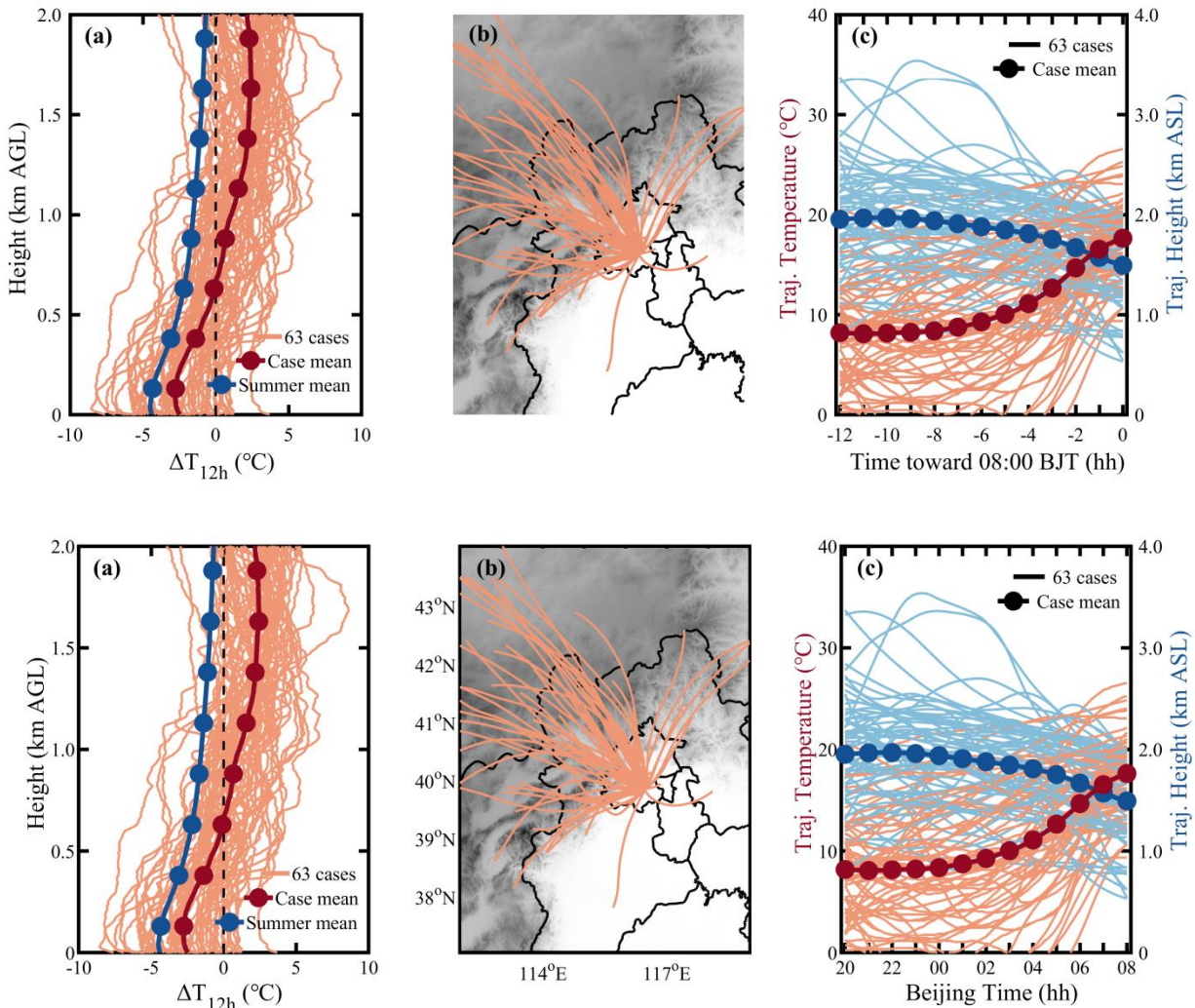
373 3.2. Climatological evaluation

374 While a case study is valuable for mechanistic understanding, the question of representativeness always arises.
 375 To clarify whether the features identified in the case study are typical, we supplemented the case analysis with a
 376 climatological investigation of elevated foehn and its O_3 pollution effect based on long-term observations.

377

378 Based on summer radiosonde data from the GXT station during 2015-2024, we calculated overnight temperature
 379 change (ΔT_{12h}) profiles for each night by differencing the temperature profiles at 20:00 BJT and 08:00 BJT the
 380 following day. We identified a residual layer warming event when $\Delta T_{12h} > 3^\circ\text{C}$ occurred within 500-2000 m height
 381 range. For each event, we identified the height of maximum warming and used it as the endpoint for backward
 382 trajectory calculations. Statistical results show that among the 920 valid summer observation days from 2015 to
 383 2024, a total of 63 residual layer warming cases were identified, accounting for 6.85% of summer night. Figure 10
 384 illustrates the ΔT_{12h} profiles, backward trajectories, and trajectory height/temperature changes for these events.
 385 While warming heights vary widely across different events, the composite ΔT_{12h} profile highlights warming above
 386 ~650 m, contrasting sharply with the summer mean profile showing nocturnal cooling throughout the layer. The
 387 backward trajectories of these warming air masses show that most originated from high-altitude regions to the west
 388 or north. After crossing the Yanshan or Taihang Mountains, these airflows arrived in Beijing, with their trajectories
 389 descending on average by 500 m and their temperature rising rapidly by an average of 10°C , exhibiting clear foehn
 390 characteristics. Applying the elevated foehn criteria from Sect. 2.2, 54 of the 63 warming cases (85.7%) can be
 391 attributed to elevated foehn. These results confirm that elevated foehn is the primary cause of nocturnal residual
 392 layer warming in Beijing.

393



394

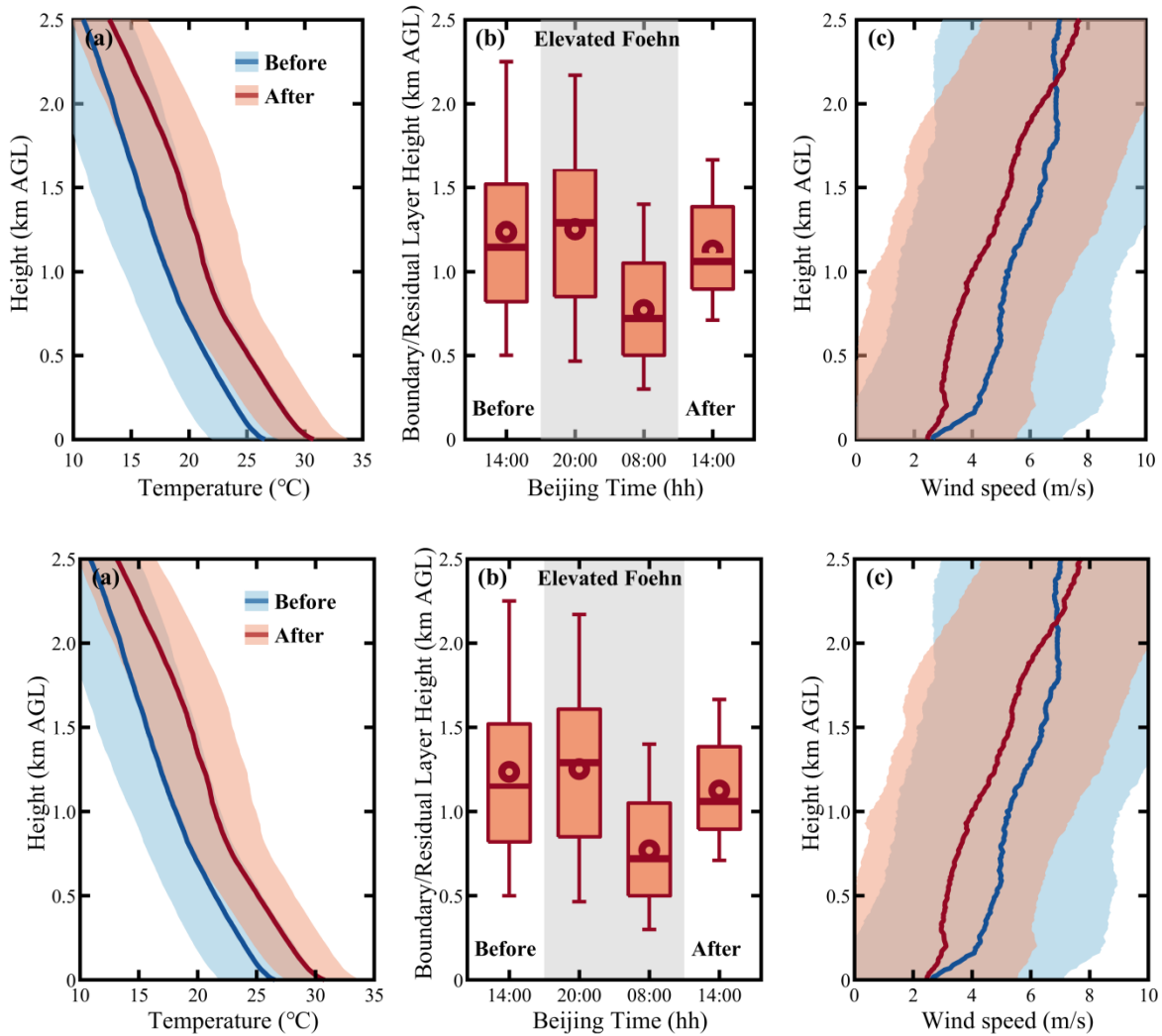
395 **Figure 10.** (a) Overnight temperature change (ΔT_{12h}) profiles from 20:00 BJT to next-day 08:00 BJT, (b) overnight
 396 airflow backward trajectories ending at the maximum warming height, and (c) overnight trajectory height and

397 temperature changes for the 63 identified residual layer warming events.

398

399 Previous case analysis indicated that elevated foehn exacerbates next-day O₃ pollution through three pathways:
400 increasing boundary layer temperature (enhancing photochemistry), reducing boundary layer height (inhibiting
401 vertical diffusion), and weakening boundary layer winds (suppressing horizontal dispersion). Composite analyses
402 of all 54 elevated foehn events (Fig. 11) strongly support the prevalence of these mechanisms. On average,
403 post-foehn afternoon boundary layer temperature was more than 3 °C higher than pre-foehn conditions. The
404 elevated foehn-induced residual layer warming directly led to an average RLH reduction of 480 m, and the
405 subsequent afternoon CBLH was, on average, 110 m lower. Post-foehn afternoon boundary layer wind speed
406 decreased by more than 1.0 m s⁻¹ on average. Overall, these meteorological changes consistently favor local O₃
407 production and accumulation. As a result, approximately 87 % of elevated foehn events were followed by worsened
408 O₃ pollution. Post-foehn MDA8O₃ concentrations across Beijing increased by an average of 20–60% (varying by
409 site) compared to the preceding day (Fig. 12b). Within the main urban zone (inside the 6th Ring Road), the
410 MDA8O₃ increase generally exceeded 45% (Fig. 12b), with concentrations commonly surpassing the national air
411 quality standard of 160 μg m⁻³ (Fig. 12a).

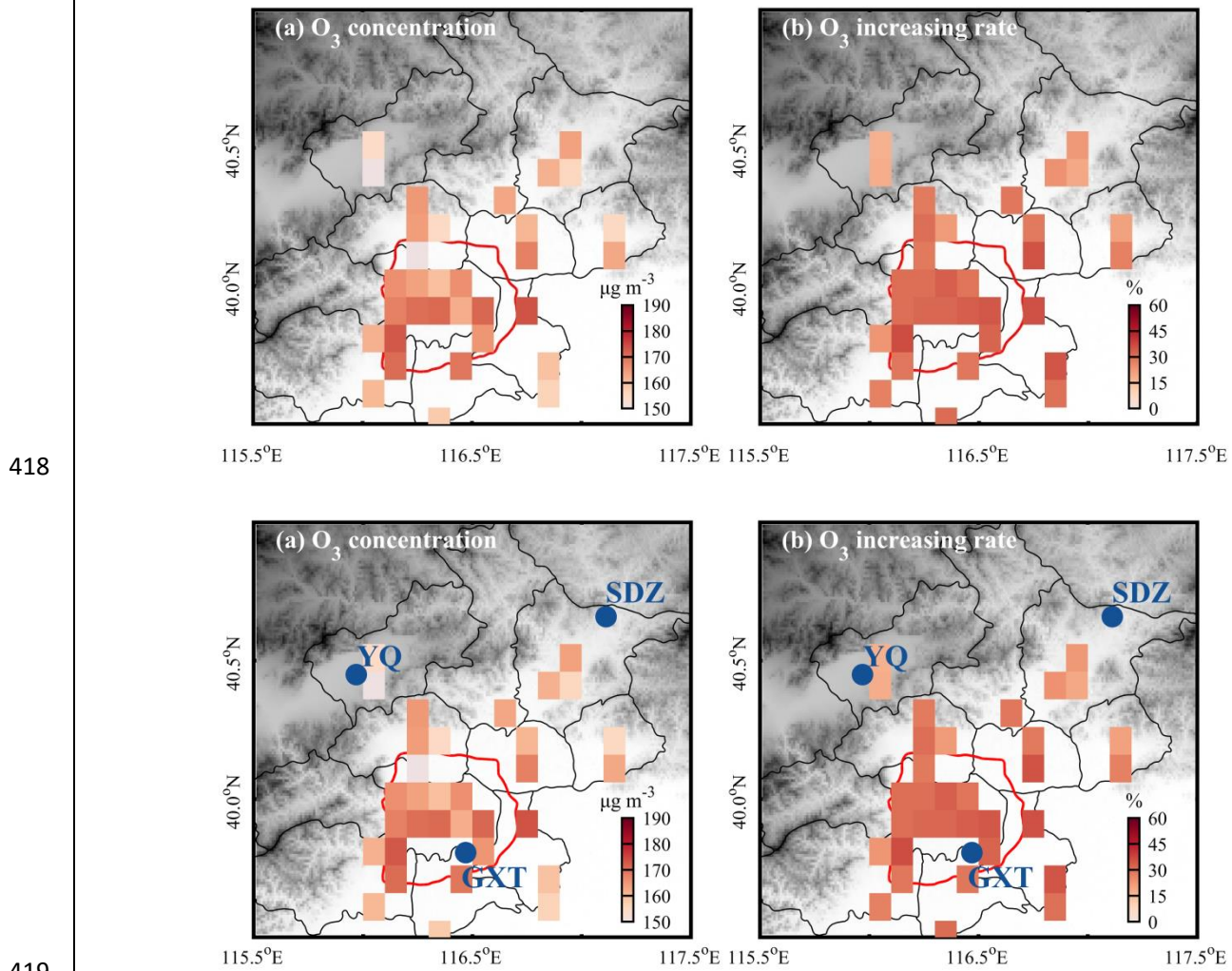
412



413

414 **Figure 11.** Composite of (a) afternoon boundary layer temperature profiles, (b) boundary/residual layer height, and
415 (c) afternoon boundary layer wind speed profiles before, during, and after 54 identified elevated foehn events in
416 Beijing. In (a) and (c), solid lines denote the mean profiles and shaded areas represent the standard deviation. In (b),

417 box-and-whisker plots show the 5th, 25th, 50th, 75th, and 95th percentiles; dots represent the means.



419
420 **Figure 12.** Composite of (a) daily maximum 8-h O₃ concentrations following elevated foehn in Beijing, and (b)
421 their average percentage increase compared to preceding days. Note: site data are resampled and shown on a
422 0.1°×0.1° grid, accounting for the relocation of some sites around 2021.

423

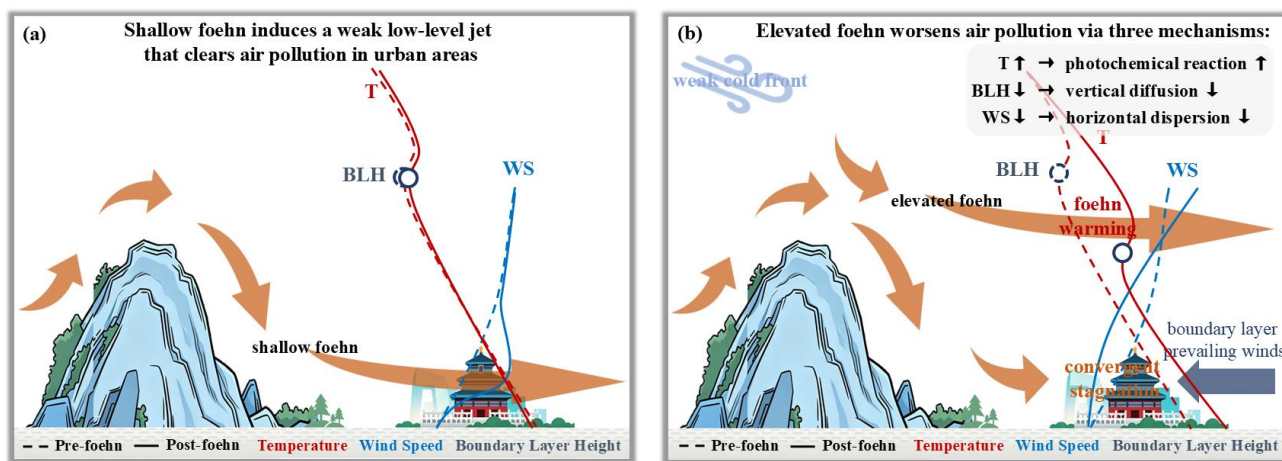
424 4. Discussion

425 Traditionally, nocturnal warming has been considered rare. Previous studies have observed occasional nighttime
426 surface warming in leeward plains or valleys due to foehn effects (Luo et al., 2020; Ma et al., 2015). This study, by
427 creatively integrating radiosonde data, reveals for the first time the frequent occurrence of pronounced nocturnal
428 residual layer warming in summer Beijing. The primary driver is identified as elevated foehn—an upper-layer
429 phenomenon previously missed by near-surface observations. Theoretically, unlike near-surface warming from
430 shallow foehn (which enhances boundary layer instability), residual layer warming from elevated foehn reinforces
431 static stability (Stull, 1988). Our observations show that ~~this~~ the elevated foehn-induced warming substantially
432 lowers the boundary layer capping inversion (i.e., RLH), thereby inhibiting the development of the next day's
433 convective boundary layer. While Pal and Lee (2019) highlighted that mountain air mass advection can lead to
434 boundary layer overrunning over downwind plains, our results demonstrate that under elevated foehn,
435 mountain-sourced air masses can instead act to lower the downwind boundary layer height through foehn warming.

436

437 The elevated foehn process in summer Beijing shows both similarities and differences with that in winter Urumqi
438 (Li et al., 2015). The similarity lies mainly in the three-layer flow structure that causes similar "sandwich" foehn
439 warming within a middle wind shear layer. The key difference lies in the post-foehn boundary layer convergence
440 mechanism. In winter Urumqi, a downslope wind and hydraulic jump occur simultaneously on the northern leeward
441 of the Tianshan Mountains after the foehn encounters a cold air pool in the southern suburbs, generating
442 convergence between the cold pool and the shallow downslope wind (Li et al., 2015). In contrast, no such cold air
443 pool exists in summer Beijing. Here, the post-foehn convergence instead results from the confrontation between the
444 emerging northwestern foehn winds and the prevailing southwestern winds within the boundary layer. The
445 relatively strong boundary-layer southwesterly winds appear to be a necessary prerequisite for the occurrence of
446 elevated foehn in summer Beijing, as they inhibit the intrusion of shallow foehn toward plain areas and, in turn,
447 force the foehn to develop upward. In other words, the relatively strong boundary-layer southwesterly winds in
448 summer Beijing likely play a role similar to that of the cold air pool in winter Urumqi in lifting the foehn to form an
449 elevated foehn.

451 Our results reveal that 86.9% of the identified elevated foehn events were followed by O₃ pollution exacerbation
452 in summer Beijing. Post-foehn MDA_{8O₃} concentrations increased more than 30% on average, exceeding the
453 national pollution threshold at most monitoring sites. In a previous study, Li et al. (2025) explored connections
454 between ground-based (shallow) foehn and PM_{2.5} pollution in Beijing, finding that 60.4 % of cases corresponded to
455 pollution mitigation and only 39.6% to exacerbation. ~~While~~ ~~Given that~~ direct comparability is limited due to
456 differences in pollutant (PM_{2.5} vs. O₃), ~~and~~ ~~season~~ (annual vs. summer), ~~and foehn type~~ (shallow vs. elevated), ~~we~~
457 acquired the summertime shallow foehn dates identified in Li et al. (2025) and conducted additional statistics of air
458 pollution for summertime shallow foehn events (Table S1). ~~the~~ The statistics indicated that elevated foehn
459 corresponds to a markedly higher probability (86.9%) of post-foehn O₃ pollution exacerbation compared to shallow
460 foehn (55.2%). Similar results are found for PM_{2.5} pollution (69.8% vs. 55.2%). ~~found in our study~~ These results
461 clearly indicates that elevated foehn exhibits a more deterministic pollution-worsened effect than shallow foehn.
462 Furthermore, we examined the changes in boundary layer structure before and after summertime shallow foehn
463 events (Fig. S5). The results revealed no significant changes in boundary layer temperature or boundary layer
464 height. However, shallow foehn tends to induce a weak low-level jet, which can clear air pollution in urban areas
465 and thereby inhibit pollution exacerbation. In light of the above comparison, we summarized a conceptual diagram
466 in Fig. 13 to illustrate the distinct pollution mechanisms associated with shallow versus elevated foehn.
467 ~~Therefore~~ Overall, elevated foehn can serve as a more reliable meteorological precursor for O₃ pollution warnings in
468 summer Beijing. ~~Notably,~~ ~~s~~Since elevated foehn can be directly identified from routine radiosonde observations
469 (Sect. 2.2), its application as a precursor for summer O₃ forecasting can be both highly convenient and timely.



470

471

472

473

474

Figure 13. Conceptual diagram illustrating the differing pollution mechanisms associated with shallow versus elevated foehn.

474

5. Conclusion

475

This study systematically investigated the formation process of elevated foehn winds and their mechanisms for exacerbating surface O₃ pollution in summer Beijing through a combined case analysis and climatological evaluation. The main conclusions are as follows:

476

477

478

479

480

481

482

483

484

485

486

487

488

489

490

491

492

493

494

495

496

497

498

499

500

501

502

- 1、 First observational confirmation of elevated foehn events in summer Beijing. Utilizing high-resolution radiosonde observations, this study identified a novel phenomenon distinct from traditional near-surface foehn. It manifests as abnormal nocturnal warming ($\Delta T_{12h} > 3\text{ }^{\circ}\text{C}$) within the elevated residual layer (approximately 500–2000 m AGL), with no significant warming signal at the surface. Lagrangian back-trajectory analysis confirms that the warming air masses originate from the northwestern or northern plateaus, undergoing descent and warming after crossing the Yanshan or Taihang Mountains, exhibiting classic foehn characteristics. These elevated foehn events account for 5.87% of summer nights and are identified as the primary driver (85.7% of identified cases) of nocturnal residual layer warming in Beijing.
- 2、 Clarification of the triple synergistic mechanisms through which elevated foehn exacerbates next-day O₃ pollution. Thermodynamic Effect I: Increasing boundary layer temperature to enhance photochemical production. Nocturnal residual layer warming directly leads to a significantly higher daytime boundary layer temperature (average increase $>3\text{ }^{\circ}\text{C}$), accelerating the photochemical reaction rates of precursors. Thermodynamic Effect II: Lowering the boundary layer height to suppress vertical diffusion. The residual layer warming reinforces atmospheric stability, causing the capping inversion base (i.e., the residual layer height) to drop by an average of $\sim 480\text{ m}$ and the subsequent afternoon convective boundary layer height to decrease by $\sim 110\text{ m}$. This substantially compresses the vertical mixing volume for pollutants. Dynamic Effect: Inducing boundary-layer convergent stagnation to weaken horizontal transport. The intruding northwesterly elevated foehn flow confronts the prevailing southwesterlies within the boundary layer, forming a convergence zone. This leads to a marked reduction in wind speed (average decrease $>1.0\text{ m s}^{-1}$), severely hindering the horizontal advective dispersion of pollutants.
- 3、 Decade-long climatological evaluation confirms the highly deterministic and prevalent exacerbating effect of elevated foehn on summer O₃ pollution. Composite analysis of 54 identified elevated foehn events from 2015–2024 robustly supports the proposed mechanisms. Statistics show that 87% of elevated foehn events were followed by worsened O₃ pollution the next day. The city-wide MDA_{8O₃} concentration increased by 20–60% on average compared to the preceding day, with increases in the main urban area typically exceeding 45%.

503 Post-foehn MDA8O₃ concentrations commonly surpassed the national ambient air quality standard (160 μg
504 m⁻³). This stands in sharp contrast to ~~previous additional~~ statistics based on near-surface observations, which
505 associate shallow foehn primarily with no significant pollution alleviation (60.4% of cases) changes,
506 highlighting the fundamental difference in pollution potential between shallow and elevated foehn.

507
508 In summary, this study identifies elevated foehn as a significant and previously overlooked meteorological
509 forcing factor for summer O₃ pollution in Beijing. Its synergistic "warming-lowering-stagnating" effects lead to a
510 highly deterministic pollution exacerbation. Given that elevated foehn can be directly identified using routine
511 radiosonde data, we propose its utility as a reliable and efficient meteorological precursor for O₃ pollution
512 forecasting and warning in Beijing and other cities with similar topography. This provides a new scientific basis for
513 the precise prevention and control of air pollution. Future research should focus on quantifying the contribution of
514 elevated foehn to O₃ generation under different synoptic backgrounds and exploring its coupling with regional
515 transport and chemical processes.

516
517 To date, numerous circulation classification-based studies have highlighted the importance of synoptic-scale
518 weather on regional O₃ pollution in the NCP region (Dong et al., 2020; Han et al., 2020; Liao et al., 2024; Liu et al.,
519 2019). However, day-to-day circulation classifications actually overlook sub-daily meteorological processes, such
520 as the nocturnal elevated foehn identified in this study. A very recent study (Xu et al., 2026) indicated that
521 ground-based foehns on the eastern Taihang Mountains preferentially occur under stable atmospheric stratification,
522 with a surface high over the windward side and a low over the leeward side, together with an upper-level cold
523 trough at 500 hPa and pronounced subsidence at 850 hPa on the leeward side on the eastern foothills of the Taihang
524 Mountains. However, this study did not extend its findings to the field of air pollution, nor did it clarify whether the
525 mentioned synoptic conditions are also conducive to the occurrence of elevated foehn. Overall, a better
526 coupling of synoptic-scale circulation patterns and local-scale elevated foehn processes will further deepen our
527 understanding of meteorological mechanisms underlying O₃ pollution.

528
529 **Data availability.** The remote sensing observations and numerical simulation results are available from the
530 correspondence author upon reasonable request (zqma@ium.cn).

531 **Author contributions**

532 Z.L. conceived the original idea, analyzed the data, and wrote the first version manuscript. J.X. conducted the
533 WRF-Chem simulation. L.Z. operated the remote sensing equipment. C.L. performed the HYSPLIT model. Z.M.
534 supervised the research project. All authors discussed the results and commented on the manuscript.

535 **Competing interests**

536 The authors declare no competing interests.

537 **Acknowledgements**

538 This research has been supported by the National Natural Science Foundation of China (Grant Nos. 42405115 and
539 42307150), and the Scientific Research Project of the Beijing Meteorological Bureau (Grant No.
540 BMBKJ202404002). We acknowledge the DeepSeek for polishing our English language. We thank the two
541 anonymous reviewers for their comments, which have greatly improved the quality of the manuscript.

542 **References**

547 Baumann, K., Maurer, H., Rau, G., Piringer, M., Pechinger, U., Prévôt, A., Furger, M., Neininger, B., Pellegrini, U., 2001.
548 The influence of south Foehn on the ozone distribution in the Alpine Rhine valley—results from the MAP field phase.
549 Atmospheric Environment 35, 6379-6390.

550 Campana, M., Li, Y., Staehelin, J., Prevot, A.S.H., Bonasoni, P., Loetscher, H., Peter, T., 2005. The influence of south foehn
551 on the ozone mixing ratios at the high alpine site Arosa. Atmospheric Environment 39, 2945-2955.

552 Dong, Y.M., Li, J., Guo, J.P., Jiang, Z.J., Chu, Y.Q., Chang, L., Yang, Y., Liao, H., 2020. The impact of synoptic patterns on
553 summertime ozone pollution in the North China Plain. Sci Total Environ 735.

554 Elvidge, A.D., Renfrew, I.A., 2016. The Causes of Foehn Warming in the Lee of Mountains. Bulletin of the American
555 Meteorological Society 97, 455-466.

556 Flowerday, C., Hansen, J.C., 2026. Peroxyacetyl Nitrate (PAN) in the Atmosphere: A Comprehensive Review of Chemistry,
557 Measurements, and Chemical-Transport Implications. Environmental Science: Atmospheres.

558 Gaffin, D.M., 2002. Unexpected Warming Induced by Foehn Winds in the Lee of the Smoky Mountains. Weather and
559 Forecasting 17, 907-915.

560 Gaffin, D.M., 2009. On High Winds and Foehn Warming Associated with Mountain-Wave Events in the Western Foothills
561 of the Southern Appalachian Mountains. Weather and Forecasting 24, 53-75.

562 Grell, G.A., Peckham, S.E., Schmitz, R., McKeen, S.A., Frost, G., Skamarock, W.C., Eder, B., 2005. Fully coupled “online”
563 chemistry within the WRF model. Atmospheric Environment 39, 6957-6975.

564 Gu, Y., Li, K., Xu, J., Liao, H., Zhou, G., 2020. Observed dependence of surface ozone on increasing temperature in
565 Shanghai, China. Atmospheric Environment 221, 117108.

566 Guenther, A., Karl, T., Harley, P., Wiedinmyer, C., Palmer, P.I., Geron, C., 2006. Estimates of global terrestrial isoprene
567 emissions using MEGAN (Model of Emissions of Gases and Aerosols from Nature). Atmos. Chem. Phys. 6, 3181-3210.

568 Han, H., Liu, J.E., Shu, L., Wang, T.J., Yuan, H.L., 2020. Local and synoptic meteorological influences on daily variability in
569 summertime surface ozone in eastern China. Atmos Chem Phys 20, 203-222.

570 Kerr, R.A., 1986. Chinook Winds Resemble Water Flowing over a Rock. Science 231, 1244-1245.

571 Kirchgaessner, A., King, J.C., Anderson, P.S., 2021. The Impact of Föhn Conditions Across the Antarctic Peninsula on Local
572 Meteorology Based on AWS Measurements. Journal of Geophysical Research: Atmospheres 126, e2020JD033748.

573 Li, J., Sun, Z., Lenschow, D.H., Zhou, M., Dou, Y., Cheng, Z., Wang, Y., Li, Q., 2020a. A foehn-induced haze front in Beijing:
574 observations and implications. Atmos. Chem. Phys. 20, 15793-15809.

575 Li, J., Zhang, J., Bai, M., Su, J., Li, Q., Jia, X., 2025. Identification and characterization of foehn events in Beijing and their
576 impact on air pollution episodes. Atmos. Chem. Phys. 25, 8683-8700.

577 Li, X., Xia, X., Wang, L., Cai, R., Zhao, L., Feng, Z., Ren, Q., Zhao, K., 2015. The role of foehn in the formation of heavy air
578 pollution events in Urumqi, China. Journal of Geophysical Research: Atmospheres 120, 5371-5384.

579 Li, X., Xia, X., Zhong, S., Luo, L., Yu, X., Jia, J., Zhao, K., Li, N., Liu, Y., Ren, Q., 2020b. Shallow foehn on the northern
580 leeside of Tianshan Mountains and its influence on atmospheric boundary layer over Urumqi, China — A climatological
581 study. Atmospheric Research 240, 104940.

582 Li, Y., Chen, M., Miao, S., Zhang, G., Huang, Q., Zhang, S., 2026. Evaluation of three scale-aware planetary boundary layer
583 schemes in WRF Model during Beijing 2022 Winter Olympics. Atmospheric Research 328, 108416.

584 Liao, Z., Pan, Y., Ma, P., Jia, X., Cheng, Z., Wang, Q., Dou, Y., Zhao, X., Zhang, J., Quan, J., 2023. Meteorological and
585 chemical controls on surface ozone diurnal variability in Beijing: A clustering-based perspective. Atmospheric
586 Environment 295, 119566.

587 Liao, Z., Sun, J., Yao, J., Liu, L., Li, H., Liu, J., Xie, J., Wu, D., Fan, S., 2018. Self-organized classification of boundary layer
588 meteorology and associated characteristics of air quality in Beijing. Atmos. Chem. Phys. 18, 6771-6783.

589 Liao, Z.H., Jia, X.C., Qiu, Y.L., Quan, J.N., Pan, Y.B., Ma, P.K., Cheng, Z.G., Wang, Q.Q., 2024. Synoptic controls on
590 warm-season O₃ pollution in eastern China: A focus on O₃-NO_x-VOC chemistry. Atmospheric Research 311, 107660.

591 Liu, J.D., Wang, L.L., Li, M.G., Liao, Z.H., Sun, Y., Song, T., Gao, W.K., Wang, Y.H., Li, Y., Ji, D.S., Hu, B., Kerminen, V.M.,
592 Wang, Y.S., Kulmala, M., 2019. Quantifying the impact of synoptic circulation patterns on ozone variability in northern
593 China from April to October 2013-2017. *Atmos Chem Phys* 19, 14477-14492.

594 Liu, S., Liang, X.-Z., 2010. Observed Diurnal Cycle Climatology of Planetary Boundary Layer Height. *Journal of Climate* 23,
595 5790-5809.

596 Luo, R., Zheng, Y., Chen, M., 2020. Mechanism of a rare night sudden intense warming event in Beijing and surrounding
597 area. *Meteorol. Monthly (in Chinese)* 46, 478-489.

598 Ma, Y., Yang, Y., Hu, X., Gan, R., 2015. Characteristics and Mechanisms of the Sudden Warming Events in the Nocturnal
599 Atmospheric Boundary Layer: A Case Study Using WRF. *Journal of Meteorological Research* 29, 747-763.

600 Miltenberger, A.K., Reynolds, S., Sprenger, M., 2016. Revisiting the latent heating contribution to foehn warming:
601 Lagrangian analysis of two foehn events over the Swiss Alps. *Quarterly Journal of the Royal Meteorological Society* 142,
602 2194-2204.

603 Ouyang, S., Deng, T., Liu, R., Chen, J., He, G., Leung, J.C.H., Wang, N., Liu, S.C., 2022. Impact of a subtropical high and a
604 typhoon on a severe ozone pollution episode in the Pearl River Delta, China. *Atmos. Chem. Phys.* 22, 10751-10767.

605 Pal, S., Lee, T.R., 2019. Advected Air Mass Reservoirs in the Downwind of Mountains and Their Roles in Overrunning
606 Boundary Layer Depths Over the Plains. *Geophysical Research Letters* 46, 10140-10149.

607 Seibert, P., Feldmann, H., Neininger, B., Bäumle, M., Trickl, T., 2000. South foehn and ozone in the Eastern Alps – case
608 study and climatological aspects. *Atmospheric Environment* 34, 1379-1394.

609 Shu, L., Xie, M., Wang, T., Gao, D., Chen, P., Han, Y., Li, S., Zhuang, B., Li, M., 2016. Integrated studies of a regional ozone
610 pollution synthetically affected by subtropical high and typhoon system in the Yangtze River Delta region, China. *Atmos.*
611 *Chem. Phys.* 16, 15801-15819.

612 Stein, A.F., Draxler, R.R., Rolph, G.D., Stunder, B.J.B., Cohen, M.D., Ngan, F., 2015. NOAA's HYSPLIT Atmospheric Transport
613 and Dispersion Modeling System. *Bulletin of the American Meteorological Society* 96, 2059-2077.

614 Steinhoff, D.F., Bromwich, D.H., Speirs, J.C., McGowan, H.A., Monaghan, A.J., 2014. Austral summer foehn winds over
615 the McMurdo dry valleys of Antarctica from Polar WRF. *Quarterly Journal of the Royal Meteorological Society* 140,
616 1825-1837.

617 Stull, R.B., 1988. *An Introduction to Boundary Layer Meteorology*; Kluwer Academic Publishers, Dordrecht, The
618 Netherlands.

619 Tang, G., Zhang, J., Zhu, X., Song, T., Münkel, C., Hu, B., Schäfer, K., Liu, Z., Zhang, J., Wang, L., Xin, J., Suppan, P., Wang, Y.,
620 2016. Mixing layer height and its implications for air pollution over Beijing, China. *Atmos. Chem. Phys.* 16, 2459-2475.

621 Wang, X.Y., Wang, K.C., 2014. Estimation of atmospheric mixing layer height from radiosonde data. *Atmos. Meas. Tech.* 7,
622 1701-1709.

623 Wu, W., Fu, T.-M., Arnold, S.R., Spracklen, D.V., Zhang, A., Tao, W., Wang, X., Hou, Y., Mo, J., Chen, J., Li, Y., Feng, X., Lin,
624 H., Huang, Z., Zheng, J., Shen, H., Zhu, L., Wang, C., Ye, J., Yang, X., 2024. Temperature-Dependent Evaporative
625 Anthropogenic VOC Emissions Significantly Exacerbate Regional Ozone Pollution. *Environmental Science & Technology*
626 58, 5430-5441.

627 Xu, J., Zhang, Z., Zhao, X., Zhang, J., 2024. Synthetically impacts of the topography and typhoon periphery on the
628 atmospheric boundary layer structure and special regional pollution pattern of O₃ in North China Plain. *Atmospheric*
629 *Environment* 330, 120566.

630 Xu, X., Shu, S., Wang, G., Li, W., 2026. Machine-learning-based identification of influencing factors and synoptic patterns
631 of foehn on the eastern foothills of the Taihang Mountains, China. *Atmos. Chem. Phys.* 26, 6507-6519.

632 Yang, X., Yang, M., Li, J., Zhang, S., 2018. Impact analysis of a Taihang Mountain foehn on haze intensity. *Meteorol.*
633 *Monthly (in Chinese)* 44, 313-319.

634 Zhang, Q., Streets, D.G., Carmichael, G.R., He, K.B., Huo, H., Kannari, A., Klimont, Z., Park, I.S., Reddy, S., Fu, J.S., Chen, D.,

635 Duan, L., Lei, Y., Wang, L.T., Yao, Z.L., 2009. Asian emissions in 2006 for the NASA INTEX-B mission. *Atmos. Chem. Phys.* 9,
636 5131-5153.

637 Zhang, S., Zeng, G., Yang, X., Wu, R., Yin, Z., 2021. Comparison of the influence of two types of cold surge on haze
638 dispersion in eastern China. *Atmos. Chem. Phys.* 21, 15185-15197.

639 Zong, L., Yang, Y., Xia, H., Yuan, J., Guo, M., 2023. Elucidating the Impacts of Various Atmospheric Ventilation Conditions
640 on Local and Transboundary Ozone Pollution Patterns: A Case Study of Beijing, China. *Journal of Geophysical Research:*
641 *Atmospheres* 128, e2023JD039141.

642